STRAIN ENGINEERING OF TWO DIMENSIONAL TRANSITION METAL DICHALCOGENIDES FOR ELECTRONIC APPLICATIONS

by

Sheng Yu
A Dissertation
Submitted to the
Graduate Faculty
of
George Mason University
in Partial Fulfillment of
The Requirements for the Degree
of
Doctor of Philosophy
Electrical and Computer Engineering

Committee:

_____ Dr. Qiliang Li, Dissertation Director

_____ Dr. Dimitris E. Ioannou, Committee Member

_____ Dr. Rao Mulpuri, Committee Member

_____ Dr. Erhai Zhao, Committee Member

_____ Dr. Monson H. Hayes, Department Chair

_____ Dr. Kenneth S. Ball, Dean, Volgenau School of Engineering

Date:_____ Summer Semester 2016
George Mason University
Fairfax, VA

Strain Engineering of Two Dimensional Transition Metal Dichalcogenides for Electronic Applications

A Dissertation submitted in partial fulfillment of the requirements for the degree of Doctor of Philosophy at George Mason University

by

Sheng Yu
Master of Microelectronics
Wuhan University, 2013
Bachelor of Electrical Science and Technology
Wuhan University, 2010

Director: Qiliang Li, Professor
Department of Electrical and Computer Engineering

Summer Semester 2016
George Mason University
Fairfax, VA

Acknowledgements

This work could not have been possible without the help and support from many people who have played an important role in my journey to obtain my PhD degree; herein, I would like to express my sincere gratitude and appreciation.

First, I would like to thank my advisor, Prof. Qiliang Li, for his guidance and support during my graduate studies at George Mason University. His solid background in semiconductor materials and devices physics left a great impact on me. I truly appreciate the time and effort that Prof. Li has committed to the achievement of this work.

I would like to extend my thanks to my colleagues at GMU, Hao Zhu, Hui Yuan, Kwesi Eshun, Chen Shi, Abbas Arab, Kai Jiang for their help, support and friendship.

My special thanks to Prof. Dimitris E. Ioannou, Prof. Rao V. Mulpuri and Prof. Erhai Zhao for the valuable knowledge I learned from them during the graduate courses they taught, and for accepting to be part of my doctoral committee.

Finally, I gratefully acknowledge the support, patience and love from my family. This work could not have been achieved without their constant encouragement and motivation.

Table of Contents

List of Tables

List of Figures

Abstract

STRAIN ENGINEERING of TWO DIMENSIONAL TRANSITION METAL DICHALCOGENIDES for ELECTRONIC APPLICATIONS

Sheng Yu, PhD.

George Mason University, 2016

Thesis Director: Dr. Qiliang Li

Two-dimensional (2D) layered materials, such as hexagonal boron nitride (h-BN) and transition metal dichalcogenides (TMDCs), have gained considerable attentions for electronic applications. Their mechanical properties, possible application in body movement, muscle stretching and blood vessel contraction, have also been studied. The MoS2 monolayer, a typical member of 2D TMDCs, becomes piezoelectric after exfoliation from the bulk crystal whereas the inversion symmetry is broken. Therefore, MoS_2 nanostructures have become promising in NEMS application in nanopiezotronics, a rapidly emerging field.

This study explicitly investigated the effect of tensile strain on 2D MoS2 monolayer using first-principle calculation. We have found that the bandgap is reduced monotonically and harmoniously by the increasing tensile strain. Two straight lines: ε_{xy} (ε_x, ε_y) with $\varepsilon_x + \varepsilon_y$ = 0.66% and $\varepsilon_x + \varepsilon_y$ = 19.06% were found as the transition boundaries between the direct and indirect bandgap structure and between the semiconductor and metal phases,

respectively. The strains along [1,0] (armchair) and [0,1] (zigzag) directions have an equal contribution to bandgap modulation. Moreover, the values of carrier effective mass along different directions behave differently under tensile strain, although they are equal to each other for biaxial strain $\varepsilon_{xy} = \varepsilon_x = \varepsilon_y$. In addition, we have found that carrier mobility can be enhanced significantly by strain and lowering temperature. Overall, this study has made a very interesting observation with detailed information on the effect of tensile strain on carrier effective mass and mobility in MoS_2 monolayer, which is very helpful for future research on monolayer MoS_2 electronics. The method and conclusion developed in this work can also benefit the research on other 2D TMDs and devices.

I have designed and simulated a novel piezoelectric device realized by MoS_2 monolayer based PN junction. Its electromechanical property was simulated by first-principle calculations. 0.31 V of output voltage can be achieved by 0.051 eV/ A^3 of the laterally tensile stress, which leads to 8% strain in transport direction. The investigation on size-dependent performance demonstrates that by increasing width, length and layer number the output will finally converge to constant output. Our investigation on the doping effect shows that various doping positions affect slightly on the output voltage and the low concentration gives rise to higher output performance. We conclude that the structure with higher EPD can obtain higher output voltage. Our study suggests a novel TMDCs PN junction and heterojunction based mechano-electric generator with high output voltage. This may open up a suite of applications in 2D-TMDCs based piezoelectric transistor.

The next focus is the interface between dielectric layer and 2D TMDC semiconductor. The interface between Al_2O_3 and MoS_2 monolayer was investigated. The evolution of

separation between Al_2O_3 and MoS_2 monolayer vs. the various thickness of dielectric layer have been studied. Also the intrinsic lattice parameter of the interface was specified by figuring out the minimum total energy. The intrinsic strain effect introduced by dielectric layer is in the range of ~0.3% to ~0.6% by varying the dielectric layer thickness of 1.3nm to 5.2nm.

One-dimensional (1D) phosphorene nanotube (PNT) is also investigated in this study. We expect that wrapping-engineering on 2D phosphorene, which models 1D phosphorene nanotube (PNT), can also tune the electrical conductance. I explicitly explored the electronic properties of armchair PNTs (APNT) and zigzag PNTs (ZPNTs) in different diameters. The strain and size effect on the bandstructure, the electron and hole effective mass and the carrier mobility are investigated for room temperature. Our study indicates that the compressive strain applied along the transport direction in our 1D structure can abate the direct bandgap as well as improve the carrier mobility of APNTs. The diameter enlargement can also enhance the electronic conductance. For the study on ZPNTs, Dirac fermions emerge at the electronic bandstructure during the wide range of lattice parameter at the transport direction. The characterization of current and voltage relation demonstrates that the conductance becomes lower as the higher diameter of ZPNT. Our observed wrapping-engineered high conductance provides many opportunities for novel applications in nano-photodetector, light-emitting diode and field-effect transistor.

Chapter 1 Introduction

1.1 Challenges and opportunities in 2D TMDCs

2D transition metal dichalcogenides (TMDCs) can provide the thinnest channel with optimized gate control for metal oxide semiconductor field-effect transistors (MOSFET). B. Radisavljevic et al. fabricated the MoS_2 monolayer based MOSFET and demonstrate effective gate control effect.[1] The starting point for the fabrication of the transistors was scotch tape-based micromechanical exfoliation of single-layer MoS_2. MoS_2 monolayers were transferred to degenerately doped silicon substrates covered with 270-nm-thick SiO_2. They proceeded with atomic layer deposition (ALD) of 30 nm HfO_2 as a high-k gate dielectric for the local top gate and mobility booster to realize the full potential of the single-layer MoS_2. The resulting structure, composed of two field-effect transistors connected in series, is shown in Fig. 1.1. I_{ds}–V_{tg} curve recorded for a bias voltage ranging from 10 mV to 500 mV, as displayed in Fig. 1.2. Measurements are performed at room temperature with the back gate grounded. Top gate width was chosen as 4 mm; top gate length was 500nm. The device can be completely turned off by changing the top gate bias from –2 to –4 V. For V_d= 10 mV, the I_{on}/I_{off} ratio is 1×10^6. For V_{ds}= 500 mV, the I_{on}/I_{off} ratio is 1×10^8 in the measured range while the subthreshold swing S= 74 mV/Vs. Top and bottom gate leakage is negligible. Inset: I_{ds}–V_{tg} for values of V_{bg}= –10, –5, 0, 5 and 10 V.

b, Ids–V_{ds} curves recorded for different values of Vtg. The linear dependence of the current on bias voltage for small voltages indicates that the gold contacts are Ohmic.

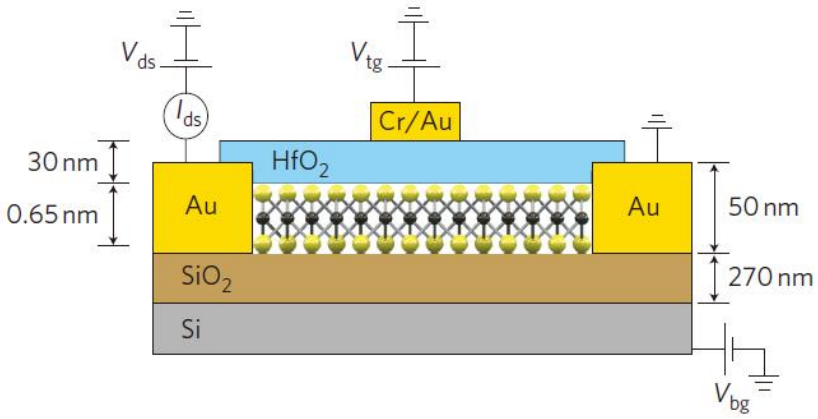

Figure 1.1 Schematic view of MoS_2 monolayer transistor

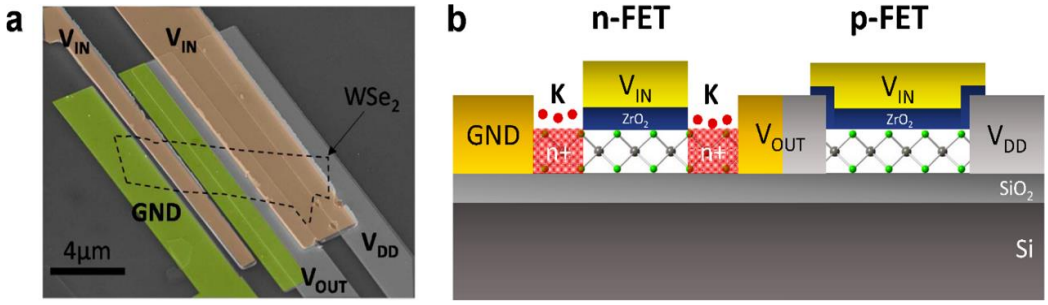

Figure 1.2 Local gate control of the MoS_2 monolayer transistor.

Mahmut Tosun et al. conduct WSe2 monolayer based complementary logic inverter [2]. In this work, the operation of n- and p-type field-effect transistors (FETs) on the same WSe_2 flake is realized and a complementary logic inverter is demonstrated. The p-FET is fabricated by contacting WSe_2 with a high work function metal, Pt, which

facilities hole injection at the source contact. The n-FET is realized by utilizing selective surface charge transfer doping with potassium to form degenerately n-type doping contacts for electron injection. An ON/OFF current ratio of $>10^4$ is achieved for both n- and p-FETs with similar ON current densities. A dc voltage gain of >12 is measured for the complementary WSe_2 inverter. This work presents an important advance toward realization of complementary logic devices based on layered chalcogenide semiconductors for electronic applications.

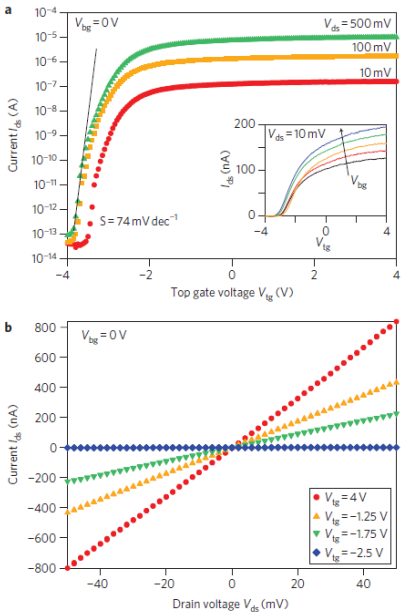

Figure 1.3 (a) False-color SEM image of a fabricated CMOS inverter on a single WSe_2 flake. (b) Schematic of the CMOS inverter, depicting the n- and p-FET components.

Figure 1.5(a) shows Photograph of the MBG device on the PEN substrate showing its outstanding flexibility and transparency. (b) Reflection mode and (c) transmission-

mode optical micrographs of the flexible and transparent MBG device [3]. Each dashed line indicates the border of each material. (d) Transfer curves of the flexible MBG device under different bending conditions up to 1.5% strain. (e) Relative field-effect mobility ($\mu/\mu 0$) of the flexible MBG device as a function of strain. The insets show the photograph of the strained MBG device by 1.5% and schematic diagram of the strained device. The arrows in the images indicate the y-direction for strain. It indicated that the carrier mobility did not increase as higher strain.

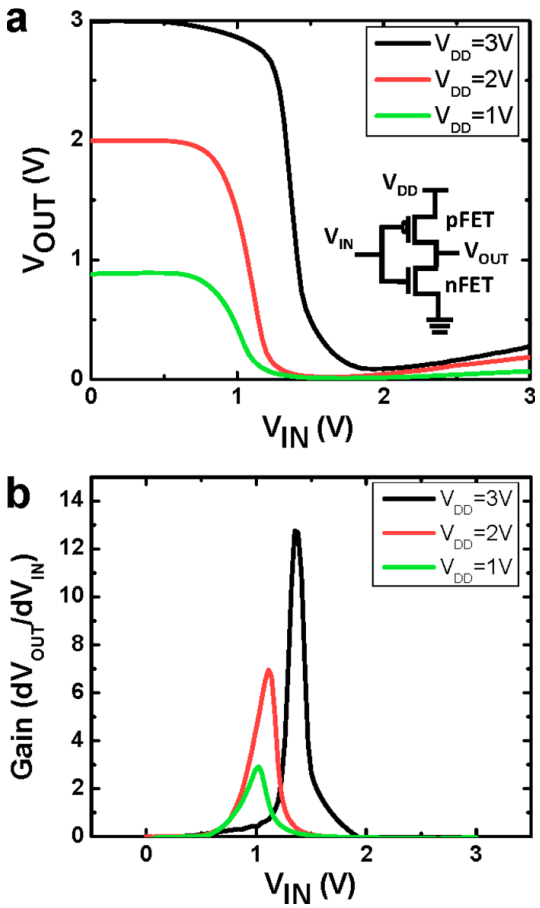

Figure 1.4 (a) Voltage transfer characteristics
(b) Direct current voltage gain of the inverter at different supply voltage

1.2 Strain-engineered TMDCs

Strain has an effective impact on the electronic, transport, and optical properties of semiconductor [4]. The strain effect is very useful when engineering one-dimensional (1D) and two-dimensional (2D) crystals because these low-dimensional structures can sustain much larger strains than bulk crystals [5] [6] [7]. For example, monolayer graphene and MoS_2 have been reported to be strained up to their intrinsic limits (~15% for graphene and ~11% for MoS_2) without substantial damage in crystal structure, enabling a dramatically wide range of tuning on the mechanical and electronic performances [7] [8]. The investigation of strain-engineering on the electronic properties of 2D crystals indicated that these materials is efficient in harvesting mechanical energy, which is a ubiquitous energy sources in the environments and readily accessible from the human activities [9] [10]. For example, mechano-electric generators built on 1D ZnO nanowires and 2D MoS_2 nanoribbons have been attracting a great deal of interest among the scientific community [11-15]. Besides device applications, a spatially modulated strain can even mimic a gauge field which is of particular importance to the study of fundamental phenomena in 2D systems. For example, strain was used to achieve ultra-strong magnetic fields and the associated zero-field quantum Hall effects as observed in graphene [16,17].

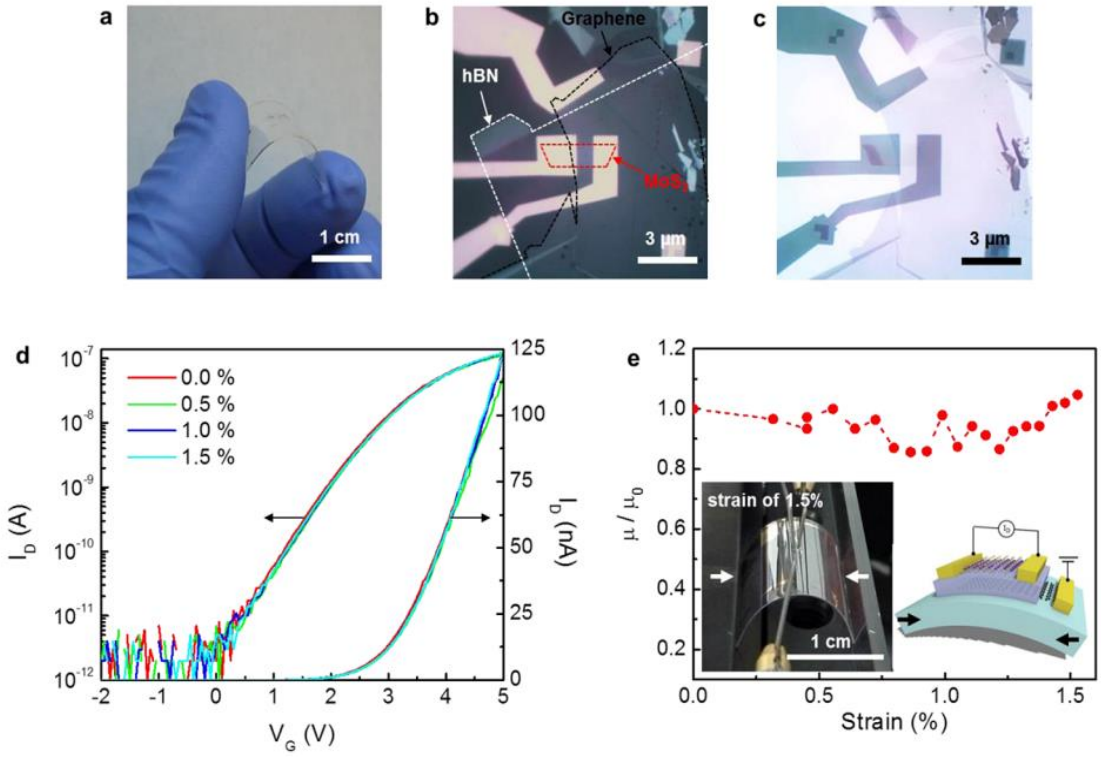

Figure 1.5 Transfer curves of the flexible MBG device under different bending and the relative field-effect mobility (μ/μ0) of the flexible MBG device as a function of strain

2D transition-metal dichalcogenides (TMDCs) have attracted intensive attention due to their novel properties that differ from their bulk counterparts [18-20]. Graphene was known to have remarkable electrical and mechanical properties, including high carrier mobility, high thermal conductance, and excellent stiffness [21-24]. However, the absence of intrinsic energy bandgap obstructs its further application in logic and memory devices which require high on-off ratio and low off-state current [25]. MoS_2, as a typical member of TMDCs, has the intrinsic direct bandgap (Eg ~ 1.8 eV) [26,27].

This makes it promising for application in future field-effect transistors (FETs) with excellent current on/off ratio (>10^8) [1,28]. However, MoS_2 monolayer has low carrier mobility, about several tens of cm^2/Vs, limiting its application in high-performance FETs [29,30]. Also, the carrier transport in these 2D monolayers is heavily affected by the scattering of the acoustic phonon via intra- and inter-valley deformation potential coupling. This further reduces the electrical conductance at room temperature (RT) [31,32]. In addition, the large variation in electrical properties induced by doping and strain in MoS_2 monolayer could affect its applications in nanoelectronics [33]. Furthermore, MoS_2 layered structures undergo transition from direct to indirect bandgap when the monolayer is stacked to multilayer structures. This restricts its applications in optoelectronic devices.

Figure 1.6 shows the atomic structure of monolayer MoS2. The (2 × 1) rectangular supercell used for elastic constants calculation is delineated by the dashed (red in the web version) line. a_x and ay are the lattice constants in the x and y directions [34]. Fig. 1.7(a) shows the plot of strain energy E_S as functions of elastic strain ε. It seems that the strain energy obeys a monotonic ascend trend as the strain increasing. By calculating the derivate of strain energy with respect to strain, we find that the harmonic region is between $0.0 < \varepsilon < 0.02$, where the structure responses to the strain linearly. Beyond the region comes into inharmonic region, higher order terms in strain energy equation are larger than 10% and can't be omitted.

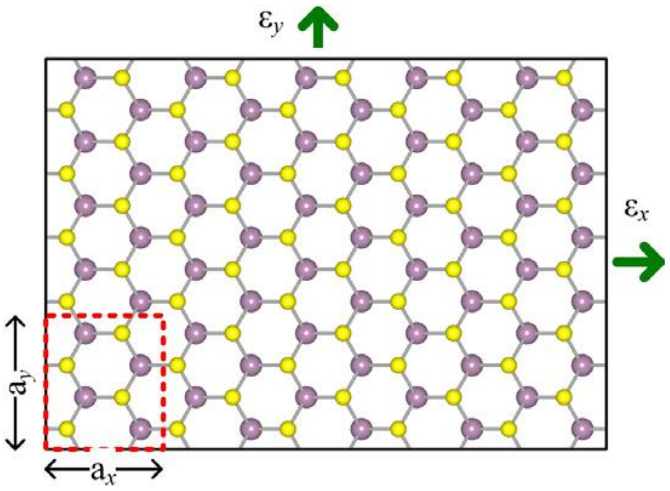

Figure 1.6 Schematic of strain engineered MoS_2 monolayer

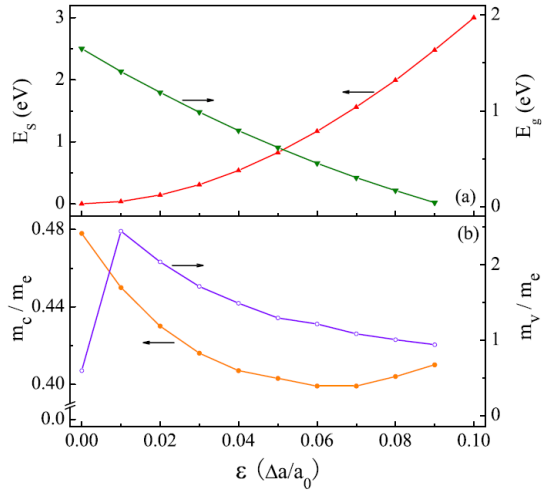

Figure 1.7 The strain energy and bandgap vs. strain and electron and hole effective mass vs. strain

The effective mass of electrons at CBM and holes at VBM in strained monolayer MoS2, is shown in Fig. 1.7(b). It is apparent that the applied strain engenders an

asymmetric influence on electrons and holes. That is, the effective mass of holes experiences an oscillation as the strain increases, whereas that of electrons displays a stable trend. The oscillation is caused by the VBM jumping from K to Γ point during strain induced deformation of band structure. Since the effective mass of holes and electrons is determined by the dispersion of energy at the VBM and CBM respectively, the jumping of VBM leads to a dramatic increase of associated effective mass value.

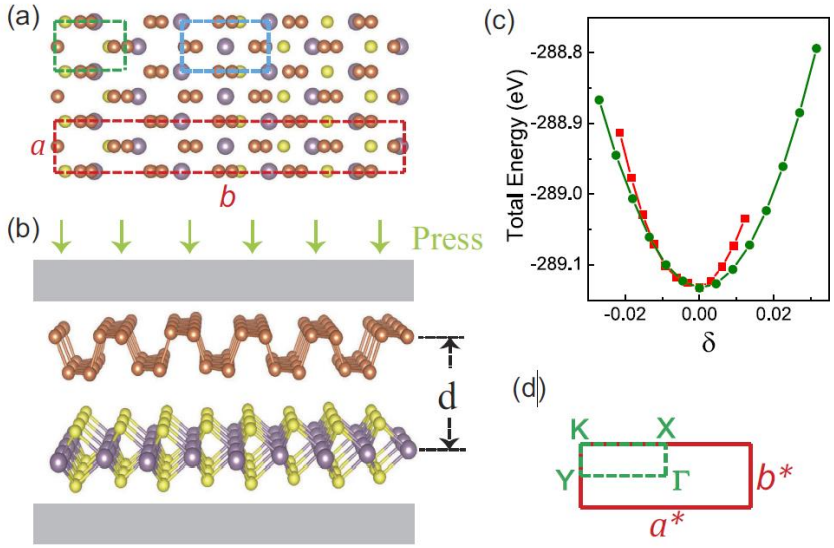

Figure 1.8 (a) Top view and (b) side view of BP/MoS2 bilayer. The green and blue rectangular regions present the unit cells of BP and MoS2. The supercell of BP/MoS2 bilayer is depicted in red rectangular region. (c) Evolution of the total energy of BP/MoS2 bilayer as a function of uniaxial strains. (d) Brillouin zone with high-symmetry points labeled.

Top and side views of the relaxed atomic structure of BP/MoS_2 bilayer are shown in Fig. 1.8 [35]. To minimize the lattice mismatch between the stacking sheets, a

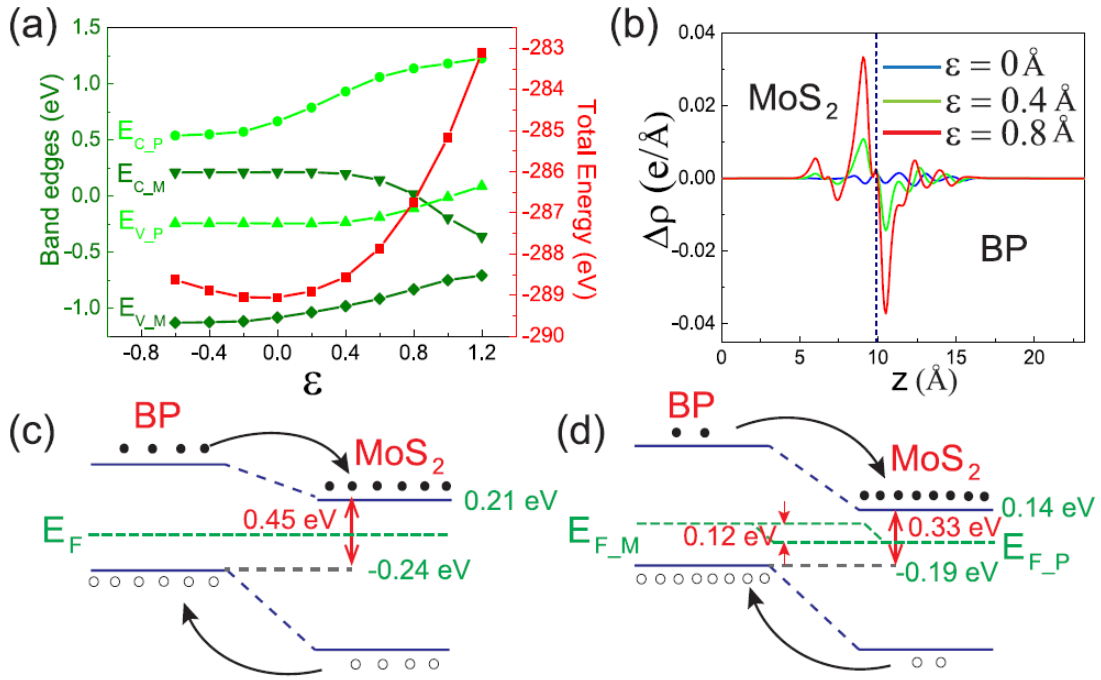

Figure 1.9 (a) Evolution of band edges and total energy of BP/MoS2 bilayer as a function of the applied compressive strain. (b) The difference between the integrated charge density of BP/MoS2 bilayer under different compressive strain and that of the isolated monolayers. (c,d) The band alignment of BP/MoS2 bilayer under applied compressive strain of 0 Å and 0.4 Å, respectively. E_f is the quasi-fermi level of BP(MoS2) in BP/MoS2 bilayer

rectangular unit cell of MoS_2 is constructed. The supercell of this system is composed by 1 × 4 unit cells of BP and 1 × 5 unit cells of MoS_2, which is the same with our previous work. The optimized lattice constants of monolayer MoS2 are a_M = 3.19 Å, b_M = 5.53 Å and the calculated lattice constants of monolayer BP are aP = 3.30 Å, bP = 4.62 Å. To determine the stable structure of BP/MoS2 bilayer, the total energy as a function of uniaxial strains along X (zigzag) and Y (armchair) directions is depicted in Fig. 1.8(c). Both curves show their minimas under zero strain, at which point, the lattice constants of

the supercell employed here are a = 3.26 Å, b = 22.18 Å. Evolution of band edges and total energy of BP/MoS2 bilayer as a function of the applied compressive strain is concluded in Fig. 1.9(a). It can be proved that the interlayer distance d0 at equilibrium state is 6.92 Å. The vdW interaction exerts little influence on the band edges of BP/MoS2. The BP/MoS2 bilayer shows a finite indirect band gap up to 0.45 eV. Upon applying compressive strain, both the VBM and CBM move towards the Fermi level, resulting in a decreasing band gap with the applied strain. The BP/MoS2 bilayer experiences a semiconductor-to-metal transition when the applied compressive strain is larger than 0.85 Å, which may lead to tunable conductivity and transport properties.

1.3 Mechanoelectric generators

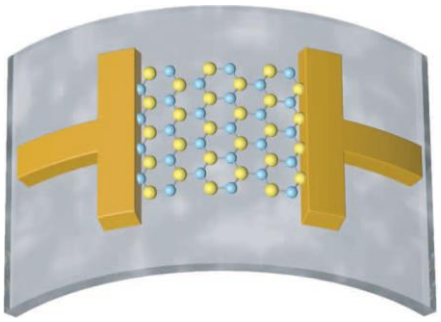

Figure 1.10 Scheme of stretched single-layer MoS2 piezoelectric device

The piezoelectric characteristics of nanowires, thin films and bulk crystals have been closely studied for potential applications in sensors, transducers, energy conversion and electronics [36]. With their high crystallinity and ability to withstand enormous strain, two-dimensional materials are of great interest as high-performance piezoelectric

materials. Monolayer MoS2 is predicted to be strongly piezoelectric, an effect that disappears in the bulk owing to the opposite orientations of adjacent atomic layers. Here we report the first experimental study of the piezoelectric properties of two-dimensional MoS_2 and show that cyclic stretching and releasing of thin MoS_2 flakes with an odd number of atomic layers produces oscillating piezoelectric voltage and current outputs, whereas no output is observed for flakes with an even number of layers.

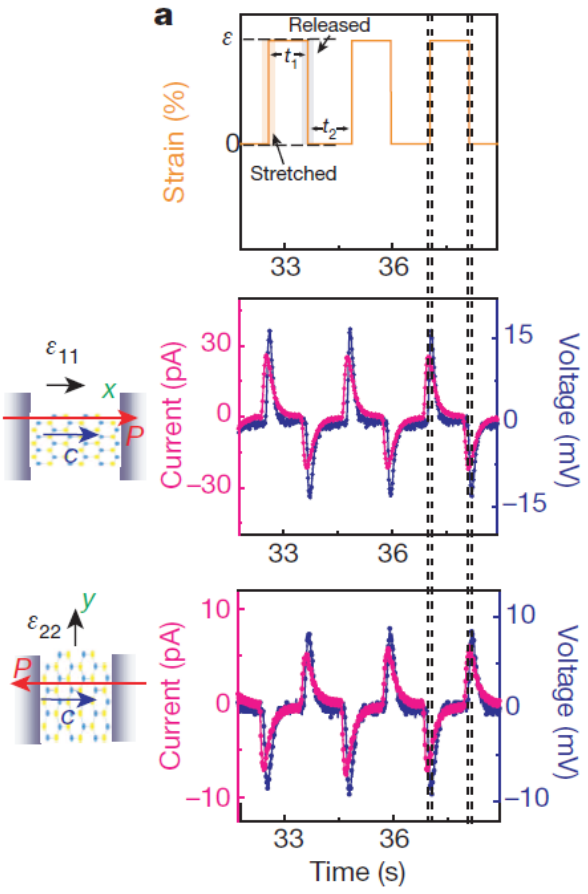

Figure 1.11 Piezoelectric outputs for single-layer MoS_2 under open-load and short circuit

A single monolayer flake strained by 0.53% generates a peak output of 15mVand 20 pA, and a 5.08% mechanical-to-electrical energy conversion efficiency. In agreement with theoretical predictions, the output increases with decreasing thickness and reverses sign when the strain direction is rotated by 906. Transport measurements show a strong piezotronic effect in single-layer MoS2, but not in bilayer and bulk MoS2. The coupling between piezoelectricity and semiconducting properties in two-dimensional nanomaterials may enable the development of applications in powering nanodevices, adaptive bioprobes and tunable/stretchable electronics/optoelectronics.

Chapter 2 Strain Effect on 2D TMDCs

2.1 Strain effect on MoS_2 monolayer

In experiment, tensile strain in MoS_2 monolayer can be achieved by stretching or bending elastomeric substrate with external stress. The strain in MoS_2 monolayer can be detected by Raman spectroscopy in which the E_{2g} mode splits and shifts due to strain [37-39]. It has been also demonstrated that strain can reduce photoluminescence and tune the polarization associated with K-K direct band gap transition. To date, many works have been reported on the simulations and modeling about the energy band structure transformation activated by strain [40]. The strain effects on electronic, optical and magnetic properties have been investigated and predicted [41]. It is widely accepted that tensile strain will cause reduction in E_g. Also, the conduction band minimum (CBM) and valence band maximum (VBM) will be overlapping each other at Fermi level under sufficiently large strain [42]. However, the distinct transition from direct to indirect bandgap structure and the transition from semiconductor to metal phase are still not clear. In addition, the low carrier mobility (μ) is one of the major barriers for the application of MoS_2 based field-effect transistor (FET). There have been found the value of μ can be enhanced to about 200 $cm^2V^{-1}S^{-1}$ by deposition of high-dielectric HfO_2 layer. In this work, we have studied the effect of tensile strain on the phase transitions, carrier effective mass and mobility in MoS_2 monolayer. The results have quantitatively demonstrated the carrier

mobility enhancement by using tensile strain, this suggesting an alternative to improve the electrical performance of MoS_2 monolayer for device application.

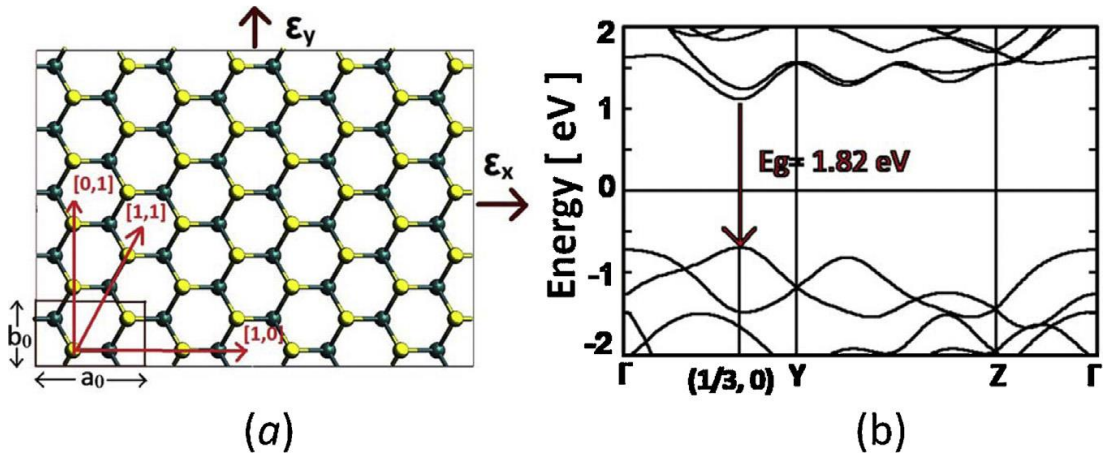

Figure 2.1.(a) Atomic structure of MoS2 monolayer. The rectangle supercell used for elastic constants calculation is delineated by the red line. (b) The band structure for unstrained MoS_2 monolayer

In this study, first principle calculations were carried out with Virtual Nanolab Atomistix ToolKit (ATK) package using density functional theory (DFT). The Localized Density Approximation (LDA) exchange correlation with a Double Zeta Polarized (DZP) basis is used with a mesh cut-off energy of 150 Ry [43]. A unit cell containing two Mo atoms and four S atoms was chosen with a periodic boundary condition. We used 1×11×11 Monkhorst-Pack k-grid mesh in this simulation [44]. All atomic positions and lattice constants were optimized by using the Generalized Gradient Approximations (GGA) with

the maximum Hellmann-Feynman forces of 0.05 eV/Å [45]. The Pulay-mixer algorithm is employed as iteration control parameter with tolerance value of 10^{-5}. The maximum number of fully self-consistent field (SCF) iteration steps is set to 100. The result of structural optimization indicated that the simple orthorhombic lattice constant a_0 = 5.47 Å, b_0= 3.16 Å, and the thickness of MoS_2 monolayer = 3.17 Å. a_0 and b_0 represent the lattice constant in armchair and zigzag directions, respectively. This optimized MoS_2 monolayer structure is in a good agreement with other publications [46].

At first, we have investigated the effect of tensile strain on the direct to indirect bandgap transition of MoS_2 monolayer. Fig. 2.1(a) shows the lattice structure of MoS_2 monolayer where the orthorhombic supercell, the smallest rectangular structure used for elastic constants calculation, is enclosed within the solid lines. The supercell built in orthorhombic way to demonstrate the carrier conduction along the armchair and zigzag directions is more intuitive than the hexagonal lattice [47]. The K point, which is defined as the fractional reciprocal coordinates (1/3, 1/3) in hexagonal lattice, is equivalent into (1/3, 0) at the midpoint between Γ-Y for orthorhombic supercell in this study. The band structure of unstrained MoS_2 monolayer is shown in Fig. 2.1(b). Its bandgap is about 1.82 eV which is in a good agreement with the previous studies. In addition, the valence band energy at Γ(0, 0) is slightly lower than the VBM at K(1/3, 0), indicating a direct bandgap at K point.

Then, we investigated the electronic properties of MoS_2 monolayer under tensile strain for different in-plane direction configurations. Strains applied along armchair and zigzag directions are noted as ε_x and ε_y, respectively. In this work, the strains are evaluated

as the lattice stretching percentage. We defined $\varepsilon_x \equiv \Delta a_0/a_0$ and $\varepsilon_y \equiv \Delta b_0/b_0$, where Δa_0 and Δb_0 are the increase of lattice constants a_0 and b_0 due to the tensile strain, respectively. A wide range of strain configurations (magnitude from 0 to 18%, in both directions) has been employed in the study. For the purpose of precision and computational efficiency, a small increment of strain, $\Delta\varepsilon$ = 0.1%, has been used to study the direct-indirect bandgap transition, while a large $\Delta\varepsilon$ = 2% has been used to study the semiconductor-metal transition.

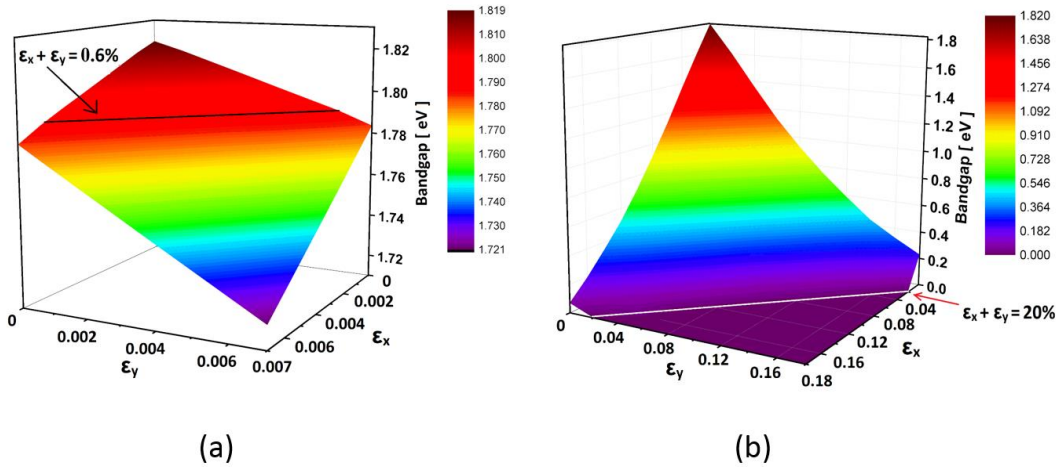

Figure 2.2 Bandgap energy with variations of strain with ε_x ($\Delta a_0/a_0$) and ε_y ($\Delta b_0/b_0$) for MoS2 monolayer (a) under small strain strength ($\varepsilon_x \leq 0.7\%,\ \varepsilon_y \leq 0.7\%$) (b) under large strain strength ($\varepsilon_x \leq 18\%,\ \varepsilon_y \leq 18\%$)

The elastic strain will induce direct to indirect bandgap transition for MoS_2 monolayer. However, very few studies have focused on the exactly detailed boundary, and

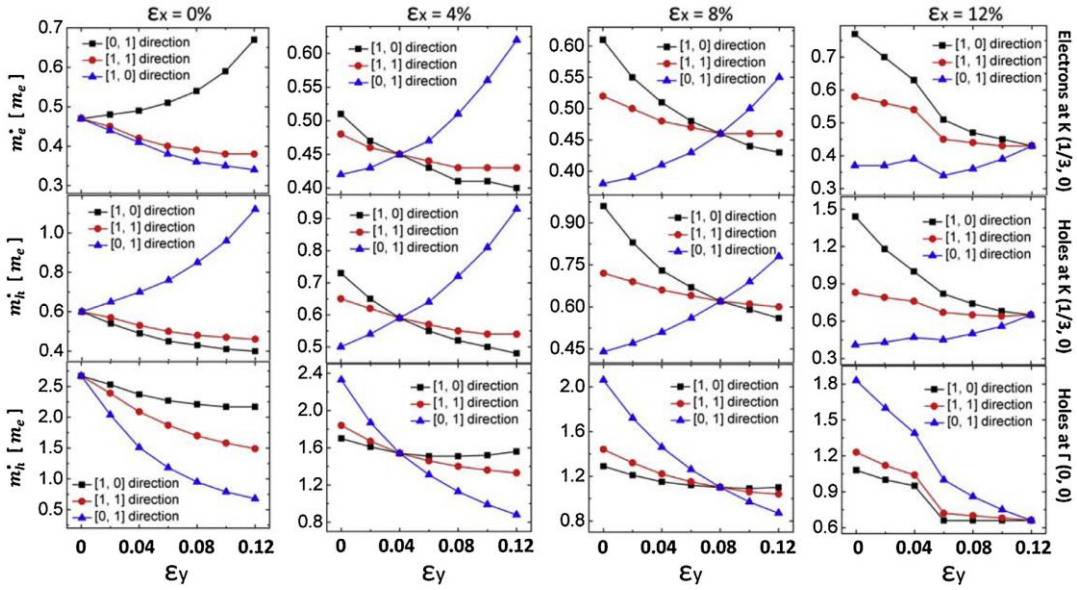

Figure 2.3 The effective mass of charge carriers as the function of strain strength ε_x and ε_y for (a) electrons at K (1/3, 0), (b) holes at K (1/3, 0) and (c) holes at Γ (0, 0).

great contradiction exists between them. T. S. Li obtained that 1% uniaxial strain is insufficient for this transition, whereas the study by W. S. Yun *et al*. showed that the critical point for direct to indirect change is 0.3%.[48] In order to make clear about this issue, we make an explicit study: monolayer MoS_2 was applied by the tensile strain in both armchair and zigzag directions by different combinations (ε_x and ε_y). The strain coefficient ε_x and ε_y are both ranging from 0 to 0.7% by $\Delta\varepsilon = 0.1\%$, totally producing 64 combinational configurations. Fig. 2.2(a) exhibits the variations of bandgap with this small strain configuration. The bandgap is reducing monotonically and linearly with increasing $\varepsilon_x + \varepsilon_y$

by the shift rate of 50 meV/%. Our simulation is in good accordance with the experimental 48 meV/% measured by C. R. Zhu. *et al.* The straight line $\varepsilon_x + \varepsilon_y = 0.6\%$ is observed as the boundary of direct to indirect transition. This is also in excellent consistence with the aforementioned report by W. S. Yun *et al.*, which indicated $\varepsilon_x = \varepsilon_y = 0.3\%$ is the critical point for this transition.

Next we turn to study the direct to indirect bandgap transition under large tensile strain. As aforementioned in order to make an explicit investigation we made a wide range of strain (from 0 to 18%) by $\Delta\varepsilon = 2\%$ in both armchair and zigzag directions, creating a mesh grid comprising 100 data points. Fig. 2.2(b) reveals the variations of bandgap energy with ε_x and ε_y. As shown the bandgap is decreasing monotonically with increasing applied strain, and vanishes when the edges of valence and conduction bands overlap the Fermi level under adequate strain. A straight line representing the boundary between the semiconductor and metal has the simple formula $\varepsilon_x + \varepsilon_y = 20\%$, implying that the strain along zigzag and armchair directions have the symmetric effect on bandgap reduction. W. S. Yun *et al.* obtained 9.8% for the transition boundary by the hexagonal lattice stretch, which is in good agreement with our study, since for his symmetrically biaxial strain, 9.8% strain strength is equivalent to 19.6% of $\varepsilon_x + \varepsilon_y$ in our simulation using simple orthorhombic lattice.

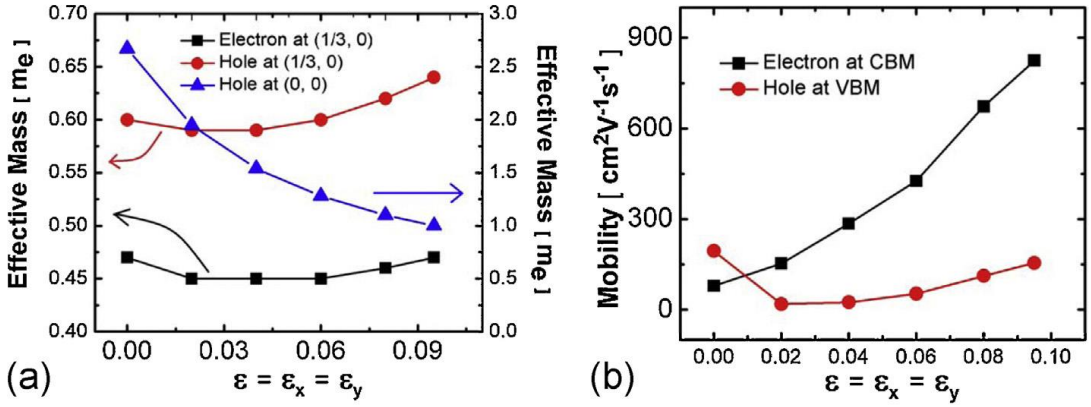

Figure 2.4(a) The effective mass of electrons and holes, (b) The mobility of electrons at CBM and holes at VBM. Both are for MoS2 monolayer under strain with $\varepsilon = \varepsilon_x = \varepsilon_y$

Strain also changes the curvature of the bands, reflected in a change in the effective masses of charge carriers. Thus we investigate the effective masses for electrons at K (1/3, 0), holes at K (1/3, 0) and Γ (0, 0) in MoS_2 monolayer under different strain combinations (ε_x, ε_y). The effective mass is calculated using $m = \hbar^2/(\partial^2 E/\partial k^2)$. Fig. 2.3 displays the dependence of the effective mass of charge carriers on the different tensile strain combinations (ε_x, ε_y): $\varepsilon_x = 0$, 4%, 8% and 12% while ε_y is changing from 0 to 12% by $\Delta\varepsilon_y = 2\%$. As shown in every panel all the three curves, which represent effective mass along [1, 0] (armchair), [0, 1] (zigzag) and [1, 1] directions respectively, surprisingly converge at a crossover point posited at $\varepsilon_x = \varepsilon_y$. The same phenomenon occurs for other strain strength of $\varepsilon_x = 2\%$, 6% and 10%. In other words, for $\varepsilon_x = \varepsilon_y$, the effective masses of charge carriers will remain the same along different directions, whereas if $\varepsilon_x \neq \varepsilon_y$, they will exhibit anisotropic behavior. Fig. 2.4(a) displays the effective masses for electrons and holes

under biaxial strain with $\varepsilon_x = \varepsilon_y$. The applied strain engenders asymmetric effect on holes at Γ (0, 0) and charge carriers at K (1/3, 0): the effective mass of holes at Γ (0, 0) decreases significantly with increasing strain, whereas they experience a slight oscillation for the charge carriers at K (1/3, 0). Our calculations obtained 0.47 and 0.60 m_e for the effective mass of electrons and holes for unstrained MoS_2 monolayer, which is consistent with previous estimation of 0.48 and 0.64 m_e.

The mobility of charge carriers play more important role in determining the induced current by external electrical field. Since the elastic strain can alter the effective mass of charge carriers, we expect their related mobility are also changing [32]. The room temperature mobility in 2D system is dominated by optical phonon scattering via intra and intervalley deformation potential couplings, which can be effectively calculated by the deformation potential (DP) theory raised by Bardeen and Shockley. Based on the effective mass approximation, the DP theory can be simplified [49] [50]:

$$\mu = \frac{2e\hbar^3 C}{3K_B T|m^*|^2 {E_1}^2}$$

where m* is the effective mass, K_B is the Boltzmann constant and T is the absolute temperature. E_1 is the DP constant which denotes the shift of the band edges (CBM for electrons and VBM for holes) induced by the strain and it can be calculated by $dE_{edge}/d\varepsilon$. C is the elastic modulus of a uniformly deformed crystal activated by the strain. For the 2D system the in-plane stiffness $C = [\partial E^2/\partial \varepsilon^2]/S_0$, where E is the total energy of supercell, ε is the strain strength coefficient, and S_0 is the area of the supercell. Q. Yue *et al.* obtained constant value 123 N/m of C,[34] which we have used in our following

calculations. Fig. 2.4(b) exhibits the mobility of electrons and holes as the function of isotropic strain with $\varepsilon = \varepsilon_x = \varepsilon_y$. As shown the mobility of electrons is enhanced dramatically as the increasing strain. However, a deep reduction of mobility for holes at VBM is observed when the strain is changing from 0% to 2%. This reduction is caused by VBM jumping from K (1/3, 0) to Γ (0, 0) during band structure deformation induced by increasing strain strength. The mobility for holes is then rapidly increasing after 2% strain, as the similar trend as that for electrons. As high as 1212 $cm^2V^{-1}s^{-1}$ of electron mobility is obtained by 10% strain and it increases over 15 times compared to 79 $cm^2V^{-1}s^{-1}$ for electrons in unstrained MoS_2 monolayer. Since high mobility means shorter switching time and higher drain-source current density, the transistor based on strained MoS_2 is expected to possess high electrical performance.

2.2 Strain Effect on ReS_2 monolayer

ReS_2 is a member of TMDCs, which has recently attracted attention on photoluminescence, Raman scattering response, and transconductive properties [51,52]. Due to the lack of interlayer registry and weak interlayer coupling arising from Peierls distortion of the 1T structure of ReS_2, the band renormalization is absent and the bulk behaves as electronically and vibrationally decoupled monolayers [53]. Consequently, the decoupled structures lead to weakly tuned bandgap by the reduced layer number: Eg=1.35 eV (bulk) and 1.43 eV (monolayer), respectively [51]. Also, from monolayers to bulk, ReS_2 remains a direct-bandgap semiconductor and its photoluminescence (PL) intensity increases with increasing number of layers. In addition, the low coupling energy (~ 18

meV per unit cell in the single layer lattice), only 8% of that of MoS_2 (460 meV), makes itself easy to be exfoliated, which is favorable for its device fabrication. Due to the stable distorted 1T phase, the reduced symmetry leads to in-plane anisotropy in various material properties leads to in-plane anisotropy in various material properties.

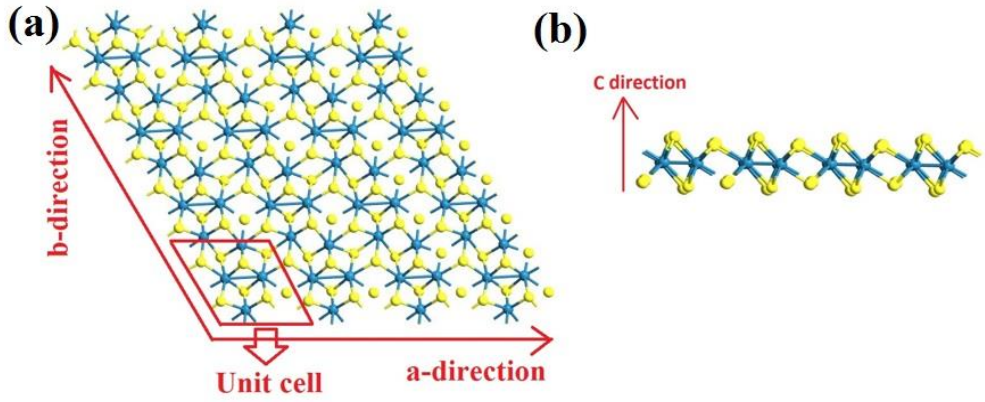

Figure 2.5 Schematic of crystalline structure of ReS_2 monolayer (a) Top view, (b) side view. The parallelogram displays the unit cell. Blue balls represent Re atoms and yellow balls represent S atoms.

Intensive studies on the anisotropic optical, electrical and Raman scattering have been recently reported. The observed anisotropic ratio in electrical conductance along two principle axes reaches 3.1, which is the highest among all known two-dimensional semiconducting materials [54]. In our study, we explicitly explore the anisotropic electronic and mechanic properties of ReS_2 monolayer by first-principle calculations. The results indicate that the strain applied in different directions can induce different elastic

modulus, band structure, effective mass and carrier mobility along different directions. In addition to a contribution to the understanding of the electronics of 2D TMDCs, our study indicates that ReS_2 layered structures have promising practical applications in photodetector, strain sensor and field-effect transistors (FETs).

In this study, first principle calculations were carried out by using the Virtual Nanolab Atomistix ToolKit (ATK) package with density functional theory (DFT). The localized density approximation (LDA) exchange correlation with a double zeta polarized (DZP) basis is used with a mesh cut-off energy of 150 Ry. The temperature is set to 300 K for our simulations on the band structure, charge carriers' effective mass and their mobility under strain effect at RT. For the investigation on the temperature dependent mobility, we set this value to 200 K, 300 K and 400 K, respectively. A unit cell containing 4 Re atoms and 8 S atoms was chosen with a periodic boundary condition. We used 11 × 11 × 1 Monkhorst-Pack k-grid mesh in this simulation. All atomic positions and lattice constants were optimized by using the generalized gradient approximations (GGA) with the maximum Hellmann-Feynman forces of 0.05 eV/Å, which is sufficient to obtain relaxed structures. The Pulay-mixer algorithmis employed as iteration control parameter with tolerance value of 10^{-5}. The maximum number of fully self- consistent field (SCF) iteration steps is set to 100. The optimized ReS_2 unit cell, which exhibits in a distorted octahedral layer structure with triclinic symmetry with lattice constant a_0= 6.51˚A, b_0= 6.41˚A, and the thickness of ReS_2 monolayer c_0 = 3.60˚A. As highlighted in Fig. 2.5(a) by the red arrows in the top view, there are two in-plane principle axes, a_0 and b_0 axes, which correspond to the second-shortest and the shortest axes in the basal plane. This optimized

monolayer structure is in a good agreement with other publications. Due to the intrinsic distorted 1T structure, ReS_2 offers an ideal candidate for investigation on the spatial anisotropic properties in 2D materials.

The components of strain along a, b and c directions are noted as ε_x, ε_y and ε_z, respectively. In this work, the strains are evaluated as the lattice stretching percentage. We defined $\varepsilon_a = \Delta a_0/a_0$, $\varepsilon_b = \Delta b_0/b_0$ and $\varepsilon_c = \Delta c_0/c_0$ where Δa_0, Δb_0 and Δc_0 are the increase of lattice constants in each direction, respectively, due to the tensile strain. We investigated the structure with tensile strain which ranged from 0 to 5% at incremental step of 1%. The mechanical property and the electronic property affected by the strain applied along three principle axes were investigated. We calculated the strain dependent elastic modulus, the band structure, the carrier effective mass and the carrier mobility along various in-plane directions. The temperature effect on carrier mobility has also been investigated.

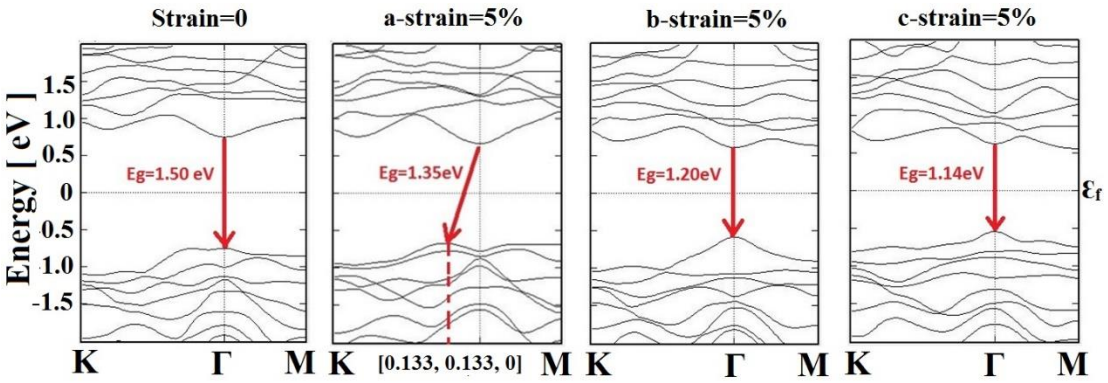

Figure 2.6 The band structure of ReS_2 monolayer applied by 0%, 5% a-direction, 5% b-direction and 5% c-direction strain, respectively.

In the first part of our study we investigated the strain effect on the electronic band structure of ReS_2 monolayer. The strain was applied along in-plane directions (a-direction, b-direction) and out-of-plane direction (c-direction). The band structure of ReS_2 monolayer under 0%, 5% strain applied along a-, b- and c-direction are displayed in Fig. 2.6, respectively. As demonstrated the ReS_2 monolayer has direct bandgap at Γ-point with value of 1.50 eV. a-direction strain induces indirect bandgap with the valence band shifting from Γ-point to [0.133, 0.133, 0] in Brillouin zone. This direct to indirect transition occurs at 1% a-direction strain. For strain along b- and c-directions, the bandgap remains direct with conduction band minimum (CBM) and valence band maximum (VBM) staying at Γ-point. The bandgap is monotonically reduced with increasing strain in each direction, whereas c-direction strain induces the most reduction in bandgap.

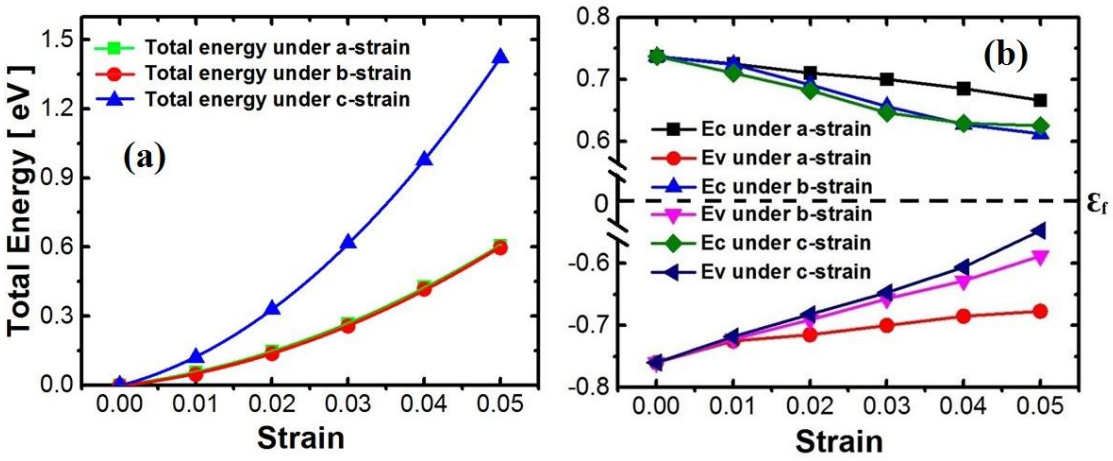

Figure 2.7 (a) The evolution of total energy of unit cell with the strain and (b) The conduction band minimum (CBM) and valence band maximum (VBM) as a function of strain.

Next we investigated the mechanical property of ReS_2 monolayer. Fig. 2.7(a) displays the total energy of the unit cell as a function of the tensile strain applied along each direction. For a 2D crystal, the elastic modulus (stiffness) $C = [\partial E2/\partial \varepsilon^2]/S_0$ [34]. S_0 is the unit cell area for 2D materials, which equals to 0.31 nm^2 in this study. The total energy vs. strain relation was fitted with quadratic parabolic curve: $E=A\varepsilon^2$. The in-plane elastic modulus C_a (a, b direction) and out-of-plane elastic modulus C_c are calculated to be 142 N/m and 352 N/m by using $C = [\partial E2/\partial \varepsilon^2]/S_0 = 2A/ S_0$. The out-of-plane elastic modulus is much higher than in-plane elastic modulus due to the much stiffer resistance in response to the applied strain along out-of-plane direction. The biaxial in-plane elastic modulus is calculated to be 284 N/m, which is much higher than other 2D TMDCs with hexagonal lattice: MoS_2 (171± 11 N/m) and WS_2 (177± 12 N/m). It should be noted that the elastic modulus of ReS_2 monolayer is approaching to that of graphene (339 ± 17 N/m), which is recognized as the material with the strongest stiffness [55].

Fig. 2.7(b) demonstrated the variation of CBM and VBM as a function of strain applied in each axis direction. Generally, the higher strain lowers CBM and raises VBM, resulting in the reduced bandgap. However, each tensile strain applied in different direction makes difference in bandgap reduction. The c-direction strain induces the most decrease in the bandgap, whereas the bandgap reduces much slower if the a-direction strain is applied. The deformation potential (DP), which is defined as the shift rate of band edge with respect to strain: $dE_{edge}/d\varepsilon$, indicates the resistance of band edge in response to the applied strain. The DP constant exhibits differently in the case of the tensile strain

applied along different directions: it is the smallest for a-direction strain while largest for c-direction strain.

Besides the total energy and bandgap, strain also changes the energy band curvature which is directly related to the carrier effective mass (m^*): $m^* = \hbar^2/(\partial^2 E/\partial k^2)$, where ħ is the reduced Planck constant, E is the energy and k is momentum. Due the 2D nature of ReS_2 monolayer, as well as the intrinsic anisotropic property, we expect

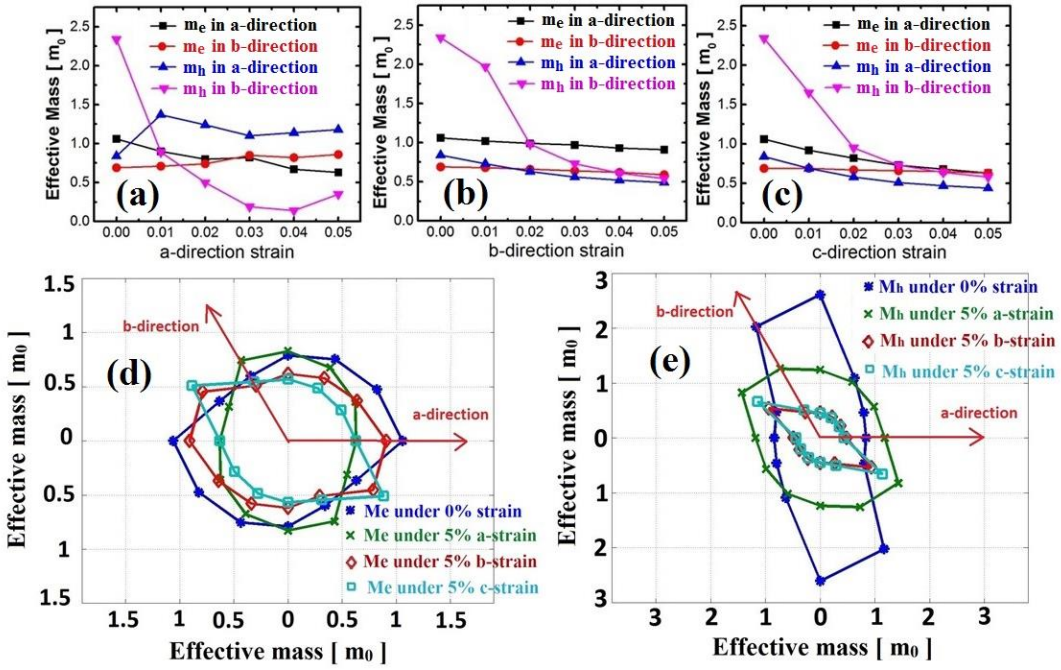

Figure 2.8 The evolution of the carrier effective mass with strain along (a) a-direction, (b) b-direction and (c) c-direction, respectively. The spatial direction dependent carrier effective mass under 0%,

that the carrier effective mass is highly anisotropic: they demonstrate different values along different spatial in-plane directions. Fig. 2.8(a), (b) and (c) demonstrates the evolution of the carrier effective mass with strain applied along a-, b- and c-direction

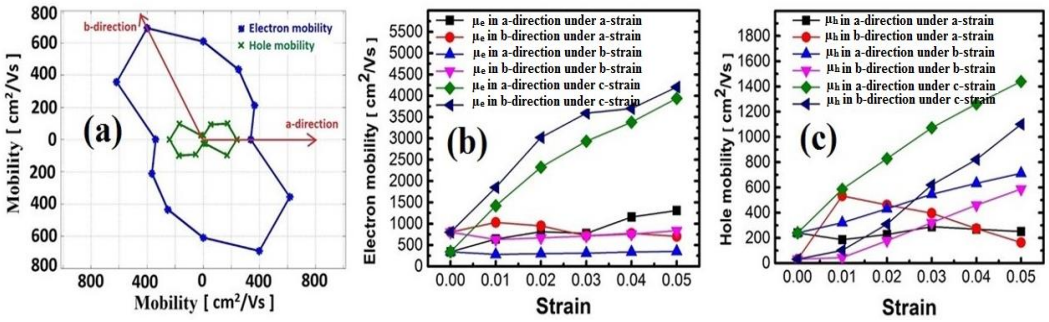

Figure 2.9 (a) The carrier mobility as a function of spatial in-plane directions for unstrained structure. The electron mobility (b) and hole mobility (c) in a- and b-direction for the structure under a-, b- and c-direction strain, respectively.

respectively. Each figure also demonstrates the strain dependent carrier effective mass in both a- and b-direction. As aforementioned a-direction strain leads to indirect bandgap that VBM shifts from Γ-point to [0.133, 0.133, 0] in the Brillouin zone and this direct to indirect bandgap transition occurs at ε_a=1%. Therefore the hole effective mass changes significantly when a-direction strain is applied from 0 to 1%: a-direction hole effective mass jumps up from 0.84m_0 to 1.37m_0 and b-direction hole effective mass reduces profoundly from 2.34m_0 to 0.81m_0. The structure remains direct bandgap when the strain is applied along b- or c-direction. Therefore we calculated the effective mass of electrons and holes at Γ-point. Generally b-direction hole effective mass is reduced the most

significantly whether for a-, b- or c-direction strain. However, the strain places limited effect on the electron effective mass. Fig. 2.8(d) and (e) display the profile of effective mass according to different spatial in-plane directions for electrons and holes, respectively. The strain doesn't give rise to a big difference in electron mobility. The hole mobility is mostly reduced in b-direction and the in-plane direction vertical to a-direction. This implies that ReS_2 monolayer has promising applications in strain sensor by using b-direction as transport direction.

The carrier mobility is a very important parameter to evaluate the electrical properties of materials. Since the carrier effective mass is affected by tensile strain, it is expected that the carrier mobility will also be affected. Kaasbjerg *et al*. have clearly shown the carrier mobility in these 2D monolayers is dominated by acoustic phonon scattering via intra- and intervalley deformation potential couplings at room temperature. The mobility can be figured out by the deformation potential (DP) theory raised by Bardeen and Shockley. Based on the effective mass approximation, the DP theory determines the mobility as:

$$\mu_{2D} = \frac{2e\hbar^3 C}{3K_B T|m^*|^2 {E_1}^2} \quad (1)$$

where e is electron charge, m* is the carrier effective mass, K_B is the Boltzmann constant and T is the temperature, E_1 is the DP constant. As aforementioned the elastic modulus C exhibits anisotropic properties where the in-plane C_a=142 N/m and the out-of-plane C_c= 352 N/m. Fig. 2.9(a) demonstrates the profile of the carrier mobility as a function of spatial in-plane directions for unstrained structure. As illustrated both the electron and hole mobility are strongly anisotropic where the electron mobility exhibits the largest along b-

direction (799.64 cm^2/Vs) and the smallest along a-direction (338.83 cm^2/Vs), while the hole mobility is the largest along a-direction (239.80 cm^2/Vs) but the smallest along b-direction (30.90 cm^2/Vs). Generally the electron mobility is much higher than hole mobility. The anisotropic ratio in electron mobility along two principle axes reaches 2.36 (b-direction mobility > a-direction mobility) while the ratio in hole mobility along these two axes is 7.76 (a-direction mobility > b-direction mobility).

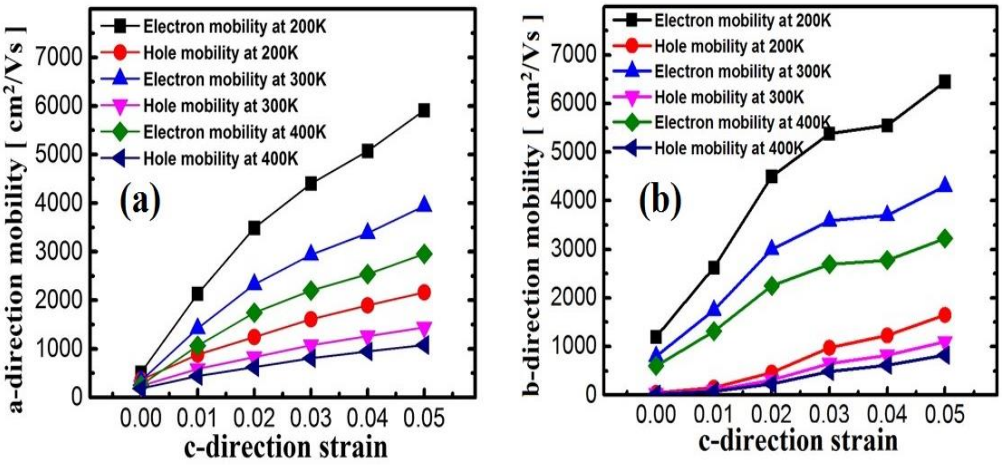

Figure 2.10 The temperature (200K, 300K and 400K) dependent carrier mobility. (a) The the electron and hole mobility in a-direction for the structure under applied c-direction strain. (b) The the electron and hole mobility in b-direction for the

Liu *et al*. reported that the conductance ratio along these two directions of ReS_2 based FET are gate dependent with values of ~ 2 when V_{bg}= 50V (where electrons are majority) and ~ 8.2 when V_{bg}= -50 V (where holes are majority) [56,57]. Our study is in good agreement

with this experimental observation. Our study suggests the conductance-switch FET based on ReS_2 monolayer tuned by gate control [58].

Fig. 2.9(b) and (c) demonstrate the electron and hole mobility along two in-plane axes affected by the applied strain in a-, b- and c-direction. The anisotropic effect is clearly shown: the carrier mobility behaves differently along different directions under applied strain with distinct directions: they are mostly boosted by c-direction strain. 5% c-direction strain can improve a-direction electron mobility from 338.83 cm^2/Vs to 3940.21 cm^2/Vs and b-direction electron mobility from 799.64 cm^2/Vs to 4300.22 cm^2/Vs. The hole mobility is also significantly improved by 5% of c-direction strain: from 239.80 cm^2/Vs to 1439.84 cm^2/Vs in a-direction and from 30.90 to 1100.76 in b-direction. This impressively enhanced carrier mobility by applied c-direction strain is mainly attributed to the significantly reduced DP constant and carrier effective mass. The hole mobility along b-direction is significantly improved by 1% a-direction strain and then reduces with the larger strain. As aforementioned, 1% a-direction strain induces the bandgap transition from direct to indirect and pushes VBM away from Γ-point. During this process the hole effective mass is significantly reduced. As 1% strain can be capably achieved in reality, we conclude that ReS_2 layered structures are very attractive for applications in the strain sensor.

We also investigated the temperature dependent carrier mobility affected by c-direction. Since the electron velocity with energy k_BT around room temperature (from 200 K to 400 K) is in the order of magnitude of 10^7 cm/s, and according to $\lambda = h/mv$, the corresponding wavelength possesses a value of several nanometers, which is much larger

than the lattice constant, thus the electron is scattered mainly by the acoustic phonons.[59] Therefore the aforementioned mathematical expression of mobility, which takes the temperature, the elastic modulus, the DP constant and the effective mass of charge carriers into account, remains good validity for our investigated temperatures. Fig. 2.10(a) and (b) separately demonstrate the c-direction boosted carrier mobility along a-direction and b-direction under different temperatures (200K, 300K and 400K). As shown they decrease monotonically as the temperature rises up. Their altered trend under applied strain shows great similarity between different temperatures: both electron and hole mobility are monotonically enhanced with larger strain. The electron mobility can achieve 5910.43 cm^2/Vs and 6449.76 cm^2/Vs when c-direction strain reaches 5%. Our study indicates $\mu \sim T^{-1}$ of temperature dependence. The relaxation time for acoustic phonon scattering is independent on the carrier energy and they exhibit temperature dependence $\mu^{-1} \sim T$. Therefore the mobility acquires $\mu \sim T^{-1}$ dependence characteristic for two-dimensional systems and layered materials dominated by acoustic phonon scattering.[60,61] It should be noted that the effective mass, deformation potential constant and elastic modulus in Eq. (1) have negligible temperature dependence.

2.3 Summary

The bandgap of MoS_2 monotonically and harmoniously reduces as the increasing strain strength. The two straight lines $\varepsilon_x + \varepsilon_y = 20\%$ and $\varepsilon_x + \varepsilon_y = 0.6\%$ are found to serve as the transition boundaries between semiconductor to metal and direct to indirect bandgap, inferring a symmetric effect by the strain along armchair and zigzag directions.

Moreover, the effective mass of carriers changes with respect to tensile strain. It is shown, for strain with $\varepsilon_x = \varepsilon_y$, they will remain the same along different directions, otherwise anisotropic character is demonstrated. By means of DP theory, the mobility for charge carriers under isotropic strain are also investigated. They are enhanced dramatically as the increasing strain strength, which is expectable for semiconductor to metal transition.

The ReS_2 monolayer exhibits different electronic properties along different directions: the electron mobility exhibits the largest along b-direction and the smallest along a-direction, while the hole mobility is the largest along a-direction but the smallest along b-direction. The strain applied along different directions induces different mechanical and electronic properties: the elastic modulus is largest for out-of-plane direction. a-direction strain induces indirect bandgap while b- and c-direction strain remain the direct bandgap. The hole effective mass along b-direction is mostly sensitive to the strain. The carrier mobility can be significantly improved by c-direction tensile strain and lower temperature. This study gives us a comprehensive understanding of strain effect on the electronic properties of ReS_2 monolayer. We also indicate that it has promising applications in nanoscale strain sensor and conductance-switch FETs.

Chapter 3 Novel Two-Dimensional Mechano-Electric Generators and Sensors Based on Transition Metal Dichalcogenides

3.1 Introduction

Mechanical energy is one of the most ubiquitous energy sources in the environments and is readily accessible from the human activities. Therefore, the conversion of mechanical energy into electricity offers an immediate, stand-alone power support for remote control systems, wearable electronics, wireless sensing and remote battery charging [62,66]. Piezoelectric transducer is the most distinguished technique for harvesting vibration based energy by its high power output and relatively low-cost manufacturing [9]. Recently, the piezoelectric properties of nanowires have been widely studied for potential applications in sensors, transducers, energy conversion and electronics [67,68]. The power generators based on piezoelectric nanostructures were successfully designed and fabricated. The coupling of semiconductor and piezoelectric properties in one-dimensional (1D) ZnO nanowires (NWs) in a nanogenerator was reported with excellent power conversion efficiency from 17% to 30% [69]. However, the difficulty in aligning 1D ZnO NWs may hinder high-performance applications in Nanoelectromechanical Systems (NEMS) [12,15].

Two-dimensional (2D) layered materials, such as hexagonal boron nitride (h-BN) and transition metal dichalcogenides (TMDCs), have gained considerable attentions for electronic applications [70,71]. Their mechanical properties, possible application in body movement, muscle stretching and blood vessel contraction, have also been studied [72]. The MoS_2 monolayer, a typical member of 2D TMDCs, becomes piezoelectric after exfoliation from the bulk crystal whereas the inversion symmetry is broken [73]. The asymmetry leads to valley polarization caused by valley-selective circular dichroism [74]. This attracts potential applications in valleytronic devices [75,76]. Therefore, MoS_2 nanostructures have become promising in NEMS application in nanopiezotronics, a rapidly emerging field [77].

The piezoelectric properties and applications of MoS_2 monolayers, such as mechanical energy harvesting and piezotronic sensing, have very recently been explored experimentally. Angular dependence of inversion symmetry has been measured by optical second-harmonic generation (SHG), indicating that it is mostly broken along armchair direction while preserves along zigzag direction. The absence of centrosymmetry endows MoS_2 monolayer with piezoelectricity along the armchair direction. An open-circuit voltage of 18mV has been demonstrated at 0.53% strain along the armchair direction[26] in a MoS_2 monolayer of a dimension of 10μm in length and 5μm in width. This output voltage is quite small. Enhancement of output performance is very important for further application of 2D materials in mechanical-to-electric generators.

In this work, we report a novel mechano-electric conversion device based on TMDC nanoribbon PN junctions and heterojunctions. As shown in Fig. 3.1(a), a TMDC

nanoribbon mechano-electric generator can be used to convert human muscle stretching power to support wearable electronics. Our first-principle calculation has shown that high output voltages, 0.036V and 0.31 V at 1% and 8% strain, respectively, can be achieved in a 1.5nm × 5nm MoS_2 nanoribbon PN junction. In consideration of the small size of nanoribbon, this mechano-electric generator has a high conversion voltage and its performance can be improved significantly by a series of connection. Our study indicates the mechano-electric conversion of 2D TMDC PN junction is better than that of the heterojunction. This work is the first study of designing 2D TMDC junctions for application in high-performance mechano-electric conversion, suggesting a new way of using 2D TMDCs for future nanogenerators and sensors.

3.2 Methods in Simulation

In this work, the energy diagrams of 2D TMDC nanoribbon PN junctions and heterojunctions have been calculated by first principle calculations carried out by the density functional theory (DFT) in Virtual Nanolab ATK package. The n-type and p-type TMDCs are achieved by substitutional doping. The Localized Density Approximation (LDA) exchange correlation with a Double Zeta Polarized (DZP) basis was used with a mesh cut-off energy of 150 Ry. We used 1×1×50 Monkhorst-Pack k-grid mesh in this simulation with more k-points in transport direction. All atomic positions and lattice constants were optimized by using the Generalized Gradient Approximations (GGA) with the maximum Hellmann-Feynman forces of 0.05 eV/Å. Pulay-mixer algorithm was employed as iteration control parameter with a strict tolerance value of 10^{-5}. The maximum number of fully self-consistent field (SCF) iteration steps was set to 1000. The electronic

temperature was set to 300K (Room temperature) for all the simulations. The self-consistent field calculations were checked strictly to guarantee fully converging within the iteration steps.

In order to clearly illustrate the design and characteristics of TMDC junction mechano-electric converters, the results are reported as follows: (1) The intrinsic piezoelectricity of 2D infinite MoS_2 monolayer was studied. (2) The PN junction-based device electric output performance was evaluated. (3) Effects of sizes (width, length and layer number) on output voltages were investigated. (4) The fluctuation in output voltage induced by various doping positions and concentrations was studied. (5) The mechano-electric conversion of TMDC nanoribbon heterojunctions were studied and compared with that of PN junctions. Finally, the mechano-electric conversion of various designs based on 2D TMDCs was analyzed and compared.

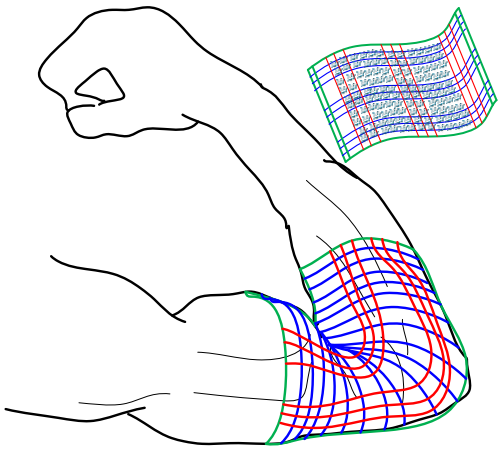

Figure 3.1 Carry-on electronics with mechano-electric generator based on 2D semiconductors

3.3 Results and Discussion

The basic MoS_2 monolayer PN junction was configured as Fig. 3.2(a). The model is divided into three regions: left electrode, right electrode, and central region. The central scattering region consists of 5×9 unit cells: the width is composed of 5 periodic unit cells in zigzag direction and 9 basic lattice lengths are included in armchair direction, which is designed as transport direction in this study. In the transport direction Dirichlet boundary condition was applied on the two opposite electrodes, in which the electric potential was held homogeneously across the boundary. Neumann condition was employed on the other two directions, in which the electric field was held homogeneously at the boundary. MoS_2 nanoribbon exhibits intrinsic semiconducting property and strongest piezoelectricity along the armchair direction while metallicity and highly crystal inversion symmetry are demonstrated in zigzag direction [78-79]. The coupled semiconducting and piezoelectric properties are responsible for the mechanism of power generator. Substituting sulfur (S) by chlorine (Cl) shifts the Fermi level towards conduction bands, resulting in n-type doping while the inverse p-type doping is realized by the replacement of phosphorus (P). The impurity density on both sides is chosen to be 10^{13} cm^{-2} within reasonable computational burden. Fig. 3.2(b) displays the electrostatic potential as a function of position in the unstrained central region. As shown it is decreasing monotonically along the transport direction and the electrostatic potential dropping (EPD) is 1.174 eV at right edge with respect to the left counterpart. This is consistent with our design that p-type is realized at the left side while the right side is n-type.

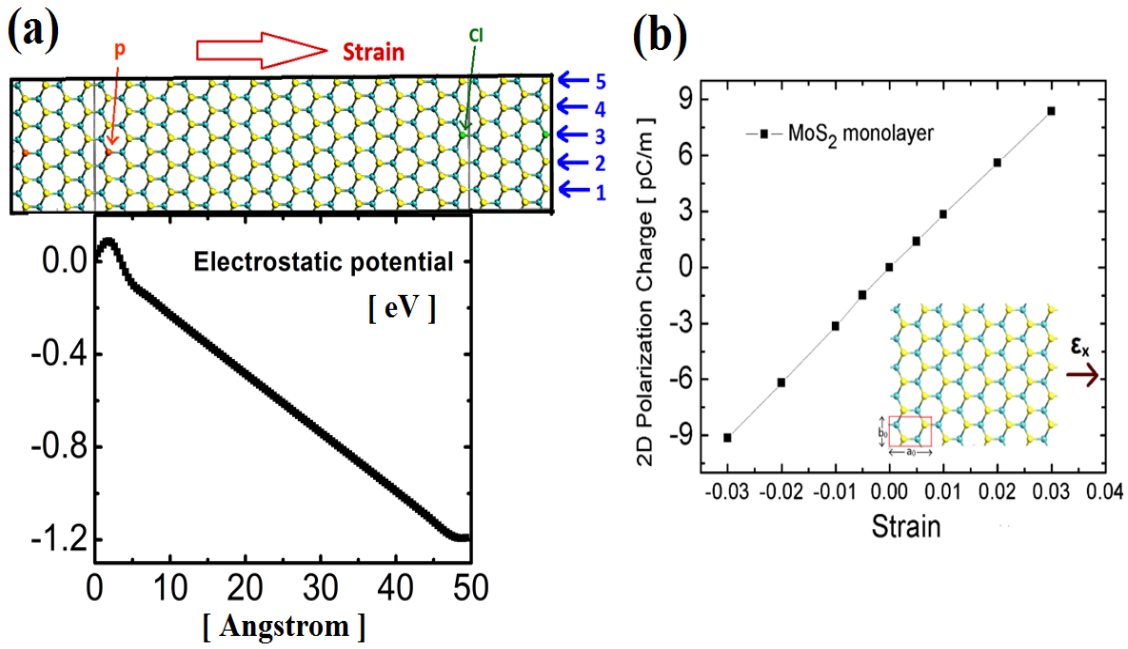

Fig. 3.2(a) Configuration of our designed device. The left and right rectangles represent the left and right electrode. (b) The electrostatic potential as a function of position in the central region under zero strain. (c)The polarization charge as the function of strain along in-plane armchair direction for undoped two dimensional infinite MoS2 monolayer. Inset: the atomic structure of MoS_2 monolayer. The strain is applied along armchair direction.

Firstly, the intrinsic piezoelectricity of MoS_2 monolayer is investigated. Noncentrosymmetric lattice structure is necessary for a material to be piezoelectric [80]. The three-dimensional (3D) bulk stacked-layer h-BN and 2H-TMDC crystals are centrosymmetric due to their experimentally observed antiparallel stacking sequence. However, the two dimensional (2D) monolayer of TMDCs, such as MoS_2, WSe_2, WS_2,

$MoSe_2$ etc., which have been successfully fabricated by exfoliation from their 3D bulk materials, exhibits noncentrosymmetric crystal structure. This noncentrosymmetry stems from the particular dislocated stacks of the different layers composed by chalcogen atoms and transition elements and accordingly results in the absence of inversion center. As a typical member of TMDCs, 2D MoS_2 monolayer is naturally piezoelectric. Figure 3.2(c) shows its polarization charge as the function of strain applied along in-plane armchair direction. In this work, the strain is evaluated as the lattice changing percentage. We defined $\varepsilon_x \equiv \Delta a_0/a_0$, where Δa_0 is the increase of lattice constant a_0 due to the strain. a_0 5.47 Å, signifying the lattice constant along the transport direction (armchair direction). The coefficient e11, defined as the slope of linear fit line for charge vs. strain curve, reveals the change in polarization along armchair direction per area by strain. Our estimation of e11 is 2.98×10^{-10} C/m, which is very close to the experimentally reported 2.90×10^{-10} C/m.

Secondly, the electronic property of our model under lateral strain has been simulated. The strain given by $\varepsilon=(L-L_0)/L_0$ is initially applied along transport direction, where L_0 and L is the equilibrium length along the transport direction of the unstrained and strained device, respectively. Fig. 3.3(a) reveals the electrostatic potential distribution along the transport

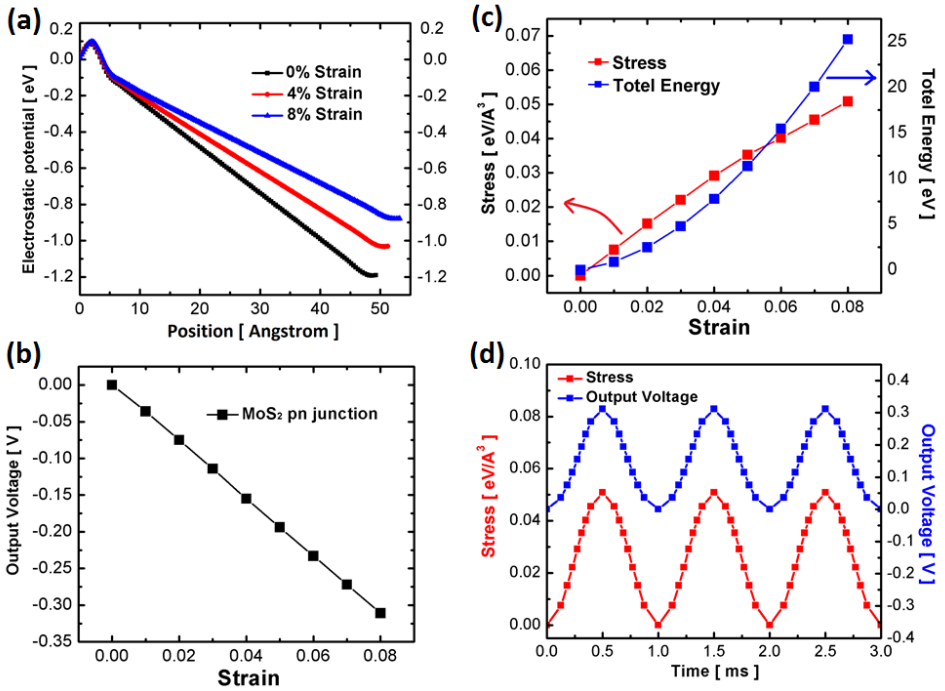

Figure 3.3 (a) 0%, 4% and 8% tensile strain modulated electrostatic potential along transport direction in the central region. (b) The output voltage as a function of strain. The negative value in our study denotes the electrical potential in left electrode is higher than right electrode. (c) The stress and total energy of the central region of our model as a function of strain. (d) Red: stress in sine waveform-time domain is laterally applied on our device. Blue: the output voltage response.

direction in the central region for the device applied by 0%, 4% and 8% tensile strain, respectively. The central region was extended from 49.2 Å to 53.2 Å in length by 8% strain. As shown the structure under 8% strain has the smallest EPD. EPD reduces from 1.174V for unstrained structure to 0.878V for the structure under 8% strain. Fig. 3.3(b) demonstrates the output voltage as a function of strain applied along the transport direction. The absolute value of output voltage is linearly increasing by larger strain. The maximum output voltage is 0.310V in the case of 8% strain. The negative value denotes

that the electrical potential at left electrode is higher than that of right electrode and therefore the left side serves as the anode while the right counterpart is the cathode in our device. Our study suggests a nano-generator with excellent performance, which has output of ~20mV in small size (5nm × 1.5nm) under 0.5% strain. This indicates significantly enhanced performance by doping and PN junction based device over undoped MoS_2 nanosheet in large area. This tremendous improvement in output is attributed to the strongly enhanced polarization between bipolar atoms induced by the coupled built-in electric field and external strain.

Next, we investigate the mechanical property of our device based on PN junction. Fig. 3.3(c) demonstrates the variation of total energy with uniaxial strain applied along transport direction. The total energy (E_{total}) is increasing monotonically as the increasing strain (ε). The slope of this curved line given by $dE_{total}/d\varepsilon$ is also rising by the increasing strain. The evolution of the stress with strain is estimated by the mathematic expression: $\sigma = \frac{1}{V} dE_{total}/d\varepsilon$, where V is the volume of our sampled system. The orthorhombic cube with the total volume of 9.6 nm^3 was sampled in our study. The stress required for deformation intensity denoted by strain ε is increasing monotonically with the larger strain. The stress vs. strain relation keeps good linearity within the small strain range $0 \leq \varepsilon \leq 3\%$ and the elastic modulus C is keeping constant by the expression: $C = d\sigma/d\varepsilon$. Previous report indicated that this parameter can remain constant within small strain ($-2\% \leq \varepsilon \leq 2\%$) for MoS_2 monolayer. For the larger strain from 4% up to 8%, this relation slightly deviates from linearity and accordingly the elastic modulus C reduces. Fig. 3.3(d) shows the output voltage response for our device under laterally applied stress in Sine

waveform-time domain. The periodic time of our dynamic stress is 1ms. Therefore a proper assumption can be suggested that there is negligible delay between input force and output voltage phase. Experimentally, the stress can be realized by bending the substrate periodically. For the mathematic expression of time dependent stress, we deduce it as following:

$$Stress = \frac{A}{2}\sin[2k\pi(t - 0.25m] + \frac{A}{2} = Asin^2(k\pi t) \quad (1)$$

where A is the maximum stress with the value of 0.051 eV/ Å^3, which induces 8% strain. As shown the maximum output voltage ~0.310V is reached at the maximum stress.

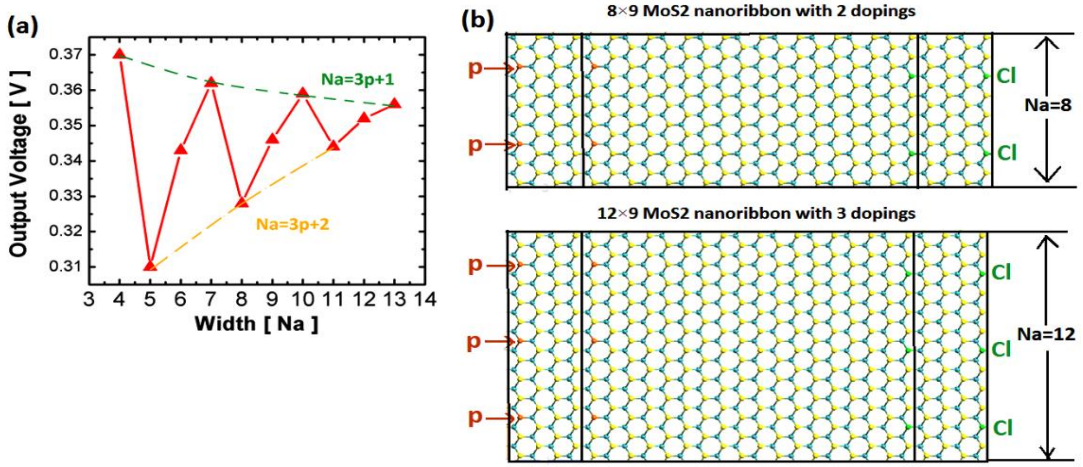

Figure 3.4 The investigation on width effect. (a) The evolution of output voltage with MoS2 nanoribbon width. All the structures are keeping one doping atom at each side. (b) Configuration of nanoribbon with width (Na=8, Na=12) by 2 doping and 3 doping atoms, respectively.

The evolution of the output voltage with the nanoribbon width (N_a) was also investigated. The nanoribbon width is denoted by periodical number of unit cells in zigzag direction vertical to the transport direction. For each structure with incremental width, one doping atom was kept at the center of lateral edge. The length of nanoribbon was kept 9 periodic unit cells in the transport direction. As displayed in Fig. 3.4(a), the output voltage oscillations are observed for the narrow ribbons, and those nanoribbons of $N_a = 3p + 1$ (where p is an integer) have larger output than the neighboring two nanoribbons. With increasing width, the output voltage finally converges to a constant value ~0.355 V. The enlarged size will attenuate the doping concentration, and might lead to unexpected impact on the performance of our device. To

clarify this issue, two pairs of phosphorus and chlorine doping atoms are introduced in 8-width structure (Fig. 3.4(b)), and also, three pairs of doping atoms are introduced in 12-width nanoribbon (Fig. 3.4(c)). The doping concentration of these structures are keeping the same as 4-width structure with one pair of doping atoms. The output voltage for these two structures are 0.328 V and 0.346 V, indicating slight difference with one doping structure of 8-width (0.328V) and 12-width (0.352V), respectively. It should be noted that the output of the structure with low doping concentration is slightly higher than that of the highly doping structure. This issue will be discussed in part **3.3.4) doping effect.**

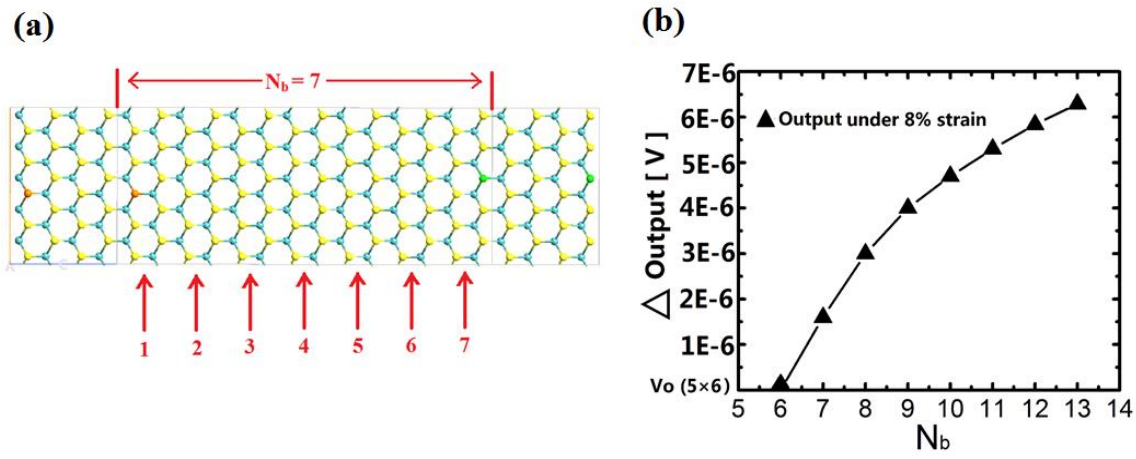

Figure 3.5 The investigation on length effect: (a) Definition of length for MoS_2 nanoribbon.
(b) Comparison of the output voltage for structures with different lengths. The output of 5×6 is 0.3103446 V, setting as the reference value.

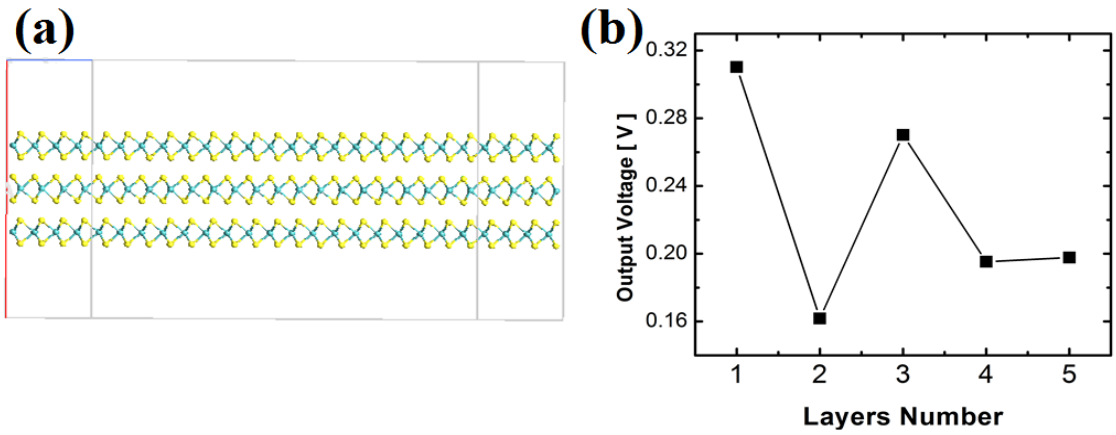

Figure 3.6 The investigation on layers effect: (a) Configuration of 3 layers MoS_2 mechano-electric converter. Each layer is doping by a pair of P and Cl, respectively.
(b) Output voltage for device under 8% strain as a function of layer number.

In addition to the width effect, we also investigate the influence of nanoribbon length on the output performance. As displayed by Fig. 3.5(a) the length of nanoribbon is defined by the periodic lattice number (N_b) of the central region in the transport direction (armchair direction). The width number (N_a) is kept constant value of 5 for all the investigations on length effect. The output voltage for the device under 8% strain as a function of N_b is shown in Fig. 3.5(b). The output voltage of the nanoribbon with N_b= 6 is 0.3103446 V, setting as the reference value. The output voltage is slightly increasing by the order of magnitude of 10^{-6} V with increasing N_b. The rising rate (ΔOutput/ΔN_b) reduces as larger N_b, indicating that the output will saturate to a constant value under sufficiently large N_b. Our study indicates that the structure length has negligible effect on the output voltage.

We also investigated the output voltage as a function of layer number of MoS_2 stacked structure. Fig. 3.6(a) shows the configuration of 3 layers MoS_2 mechano-electric converter. Each layer is doping by a pair of P and Cl, respectively. P replaces S at left side while Cl is

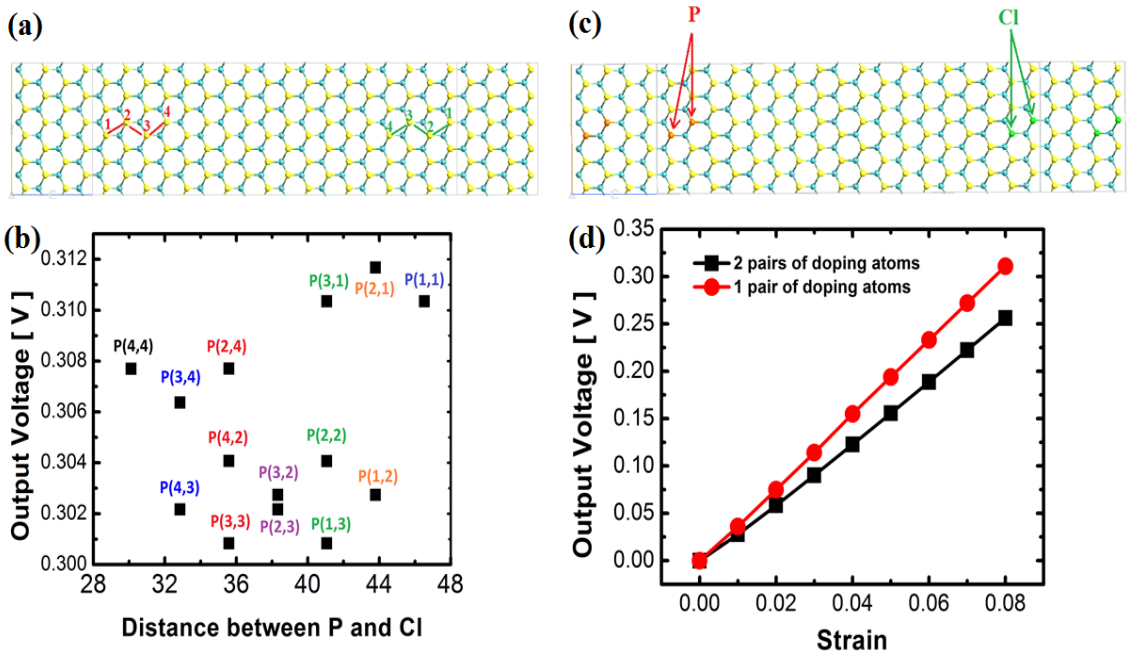

Fig. 3.7 The investigation on doping effect:
(a) The various combinational doping positions of P and Cl, denoted by P(m, n). As displayed, m, n are the atomic ordinal of P and Cl. (b) The output voltage (under 8% strain) as a function of doping position P(m, n). (c) Configuration of 2 pairs of doping atoms. (d) Comparison of output performance between 2 pairs of doping and 1 pair

doping at right side. As demonstrated by Fig. 3.6(b), the output voltage exhibits a fluctuant behavior as increasing layers. It reaches maximum of 0.310V by single layer, while is reducing significantly to 0.16V by 2 layers stacked structure. As limited by the simulation complexity and its converging difficulty, we only put forward our investigation to 5 layers. However, a reasonable speculation can be made that the output voltage finally converges to a constant value as increasing layer number, which is trended similarly as that tuned by increasing width. In experiments the output voltage of undoped MoS_2 in large area shows a proportional relation with the second-harmonic generation (SHG) intensity for stacked

structures: MoS_2 flakes stacked by odd number of layers exhibited strong piezoelectricity along armchair direction, while the output voltage disappeared for even number of layers. Our study shows that the structures with even number of layers still have strong output, indicating a distinct underlying physical principle with the device by undoped nanosheet. It should be noted that as the larger size (Larger width, length and layer number), the output voltage of our device tends to converge to a constant value. Our study suggests a mechano-electric generator with weak dependence on dimension and size, which is exceedingly favourable for industrial application.

Precisely control the dopant position and number is the main challenge for the application of low-dimensional nanomaterials. This inaccuracy in fabrication induces variations in mechanic and electronic properties of 2D materials and devices. Therefore we investigate the variation of output voltage upon the various doping positions in MoS_2 nanoribbon mechano-electric converter. As displayed by Fig. 3.7(a), the various combinational doping positions of P and Cl are denoted by P(m, n), where m, n are the atomic ordinal number of doping atoms P and Cl. P replaces S at left side while Cl is doping at right side. The variation of output voltage upon the doping combinations is exhibited in Fig. 3.7(b). The combination P(4,4) has the nearest distance between P and Cl while they reaches farthest away from each other in P(1,1). Generally the output voltage randomly fluctuates within small range from 0.301V to 0.312V. This limited variation modulated by various doping positions is favourable for future industrial applications. The doping concentration effect are also revealed in our study. 2 pairs of doping atoms are introduced in our device, as shown in Fig. 3.7(c). The dependence of output voltage on

strain is demonstrated in Fig. 3.7(d). It increases linearly as larger strain. However, the output is lowered by higher doping concentration compared to that of the device based on one pair of doping atoms. The output is 0.028V and 0.256V for the device applied by 1% and 8% strain, respectively.

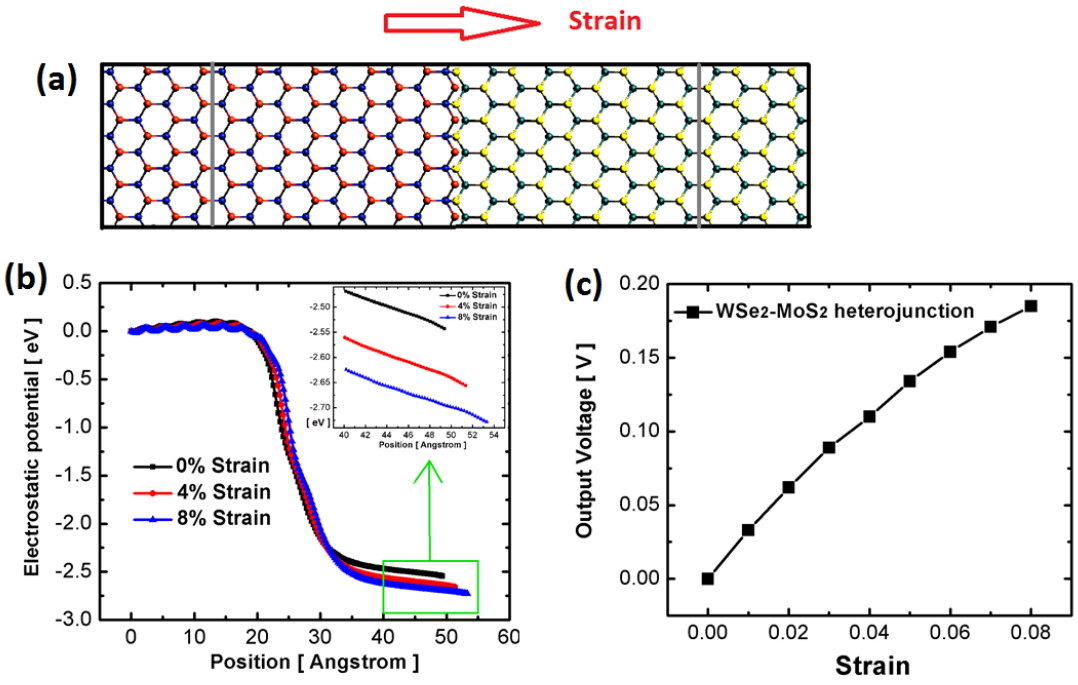

Figure 3.8(a) Configuration of nano-power generator based on WSe2 and MoS2 heterojunction. The left part consists of WSe2 and the right part is MoS2.
(b) 0%, 4% and 8% tensile strain modulated electrostatic potential along transport direction in the central region for device displayed in Fig. 5(a). Inset: the enlarged view of electrostatic potential within the region from 40Å to 55Å. (c) The evolution of the output voltage with strain.

We also investigate the mechano-electric converter based on TMDCs heterojunctions. Fig. 3.8(a). displayed the WSe_2-MoS_2 heterojunction based mechano-electric generator. The left part is WSe_2 nanoribbon and the right counterpart is MoS_2 nanoribbon. Fig. 3.8(b)

reveals the electrostatic potential distribution along transport direction in the central region for the device under 0%, 4% and 8% tensile strain, respectively. The EPD mainly occurs at the narrow connection region between WSe_2 and MoS_2 nanoribbon. This radical change

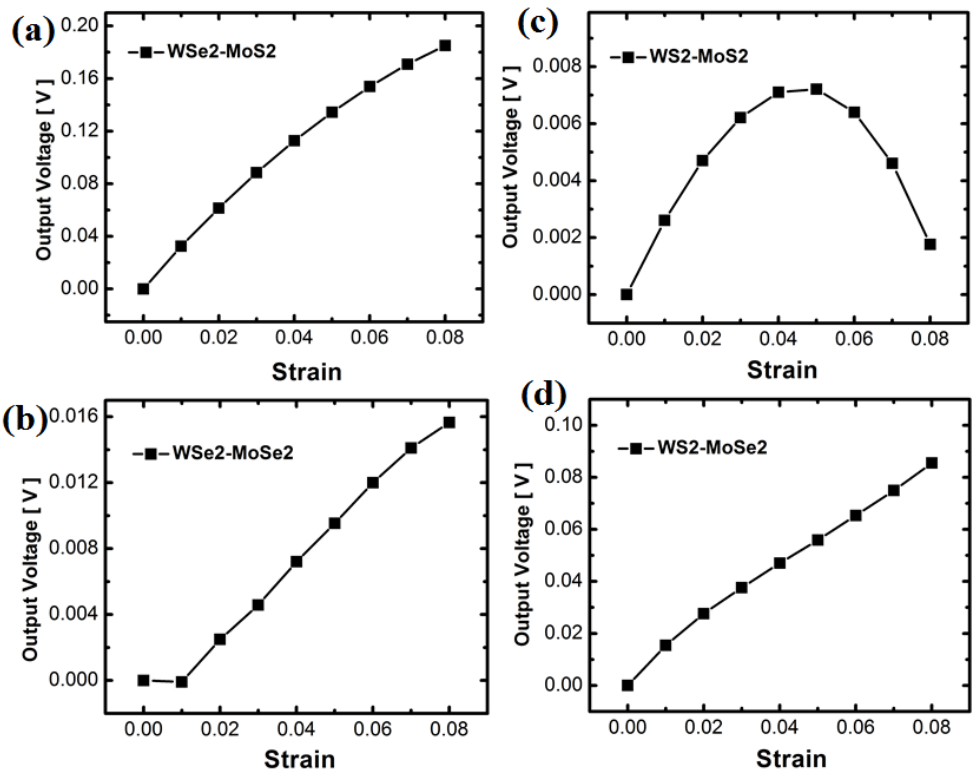

Figure 3.9 The output voltage as a function of strain for 4 heterojunction structures: (a) WSe_2-MoS_2 (b) WSe_2-$MoSe_2$ (c) WS_2-MoS_2 (d) WS_2-$MoSe_2$

in electrostatic potential arises from the great difference between the work functions of WSe_2 and MoS_2 monolayer. As opposite to the regulatory change of EPD by strain in MoS_2 PN junction, increasing strain causes larger EPD in heterojunctions. Fig. 3.8(c) reveals the

output performance as a function of strain. The output voltage increases with larger strain and 0.185V can be achieved by 8% strain. Our observation suggests that MoS_2 PN junction based device has better output performance than TMDCs based heterojunctions.

Fig. 3.9 shows the output voltage as a function of strain for 4 different heterojunctions: a) WSe_2-MoS_2 (b) WSe_2-$MoSe_2$ (c) WS_2-MoS_2 (d) WS_2-$MoSe_2$. As shown in Fig. 3.9(c), WS_2-MoS_2 heterojunction reaches maximum output of 7.21×10^{-3} V under 5% strain, then reduces significantly by larger strain. For the other 3 structures, the output voltage is generally increasing by larger strain. Among these structures, WSe_2-MoS_2 heterojunction achieves the largest output of 0.185V under 8% strain. However, this is still inferior to the performance of MoS_2 PN junction, which possesses the output of 0.310V under the equal strain. WSe_2-MoS_2 and WS_2-$MoSe_2$ can obtain the output voltage with a value of one order of magnitude larger than those of the other two structures, indicating that the enhanced output can be achieved by the TMDCs heterojunction based on different chalcogen materials. Table 1 summarizes the output voltage and EPD for 8 different TMDCs PN junctions and heterojunctions, all of which are in the same size of 5×9 (N_a=5, N_b=9). The heterojunction structures with higher EPD can achieve higher output voltage. Larger EPD is attributed to larger difference in work functions of distinct nanoribbons at opposite sides. This rule is also applied appropriately to the TMDCs PN junctions, among which the output voltage and EPD both reach largest value in WS_2 PN junction.

Table 1. The comparison of output voltage and EPD for different structures.

Strain=8%	Output [V]	EPD [eV]
MoS_2 PN junction	0.310	1.174
WSe_2 PN junction	0.328	1.089
$MoSe_2$ PN junction	0.189	0.992
WS_2 PN junction	0.356	1.369
WSe_2-MoS_2 heterojunction	0.185	2.543
WS_2-MoS_2 heterojunction	0.00721	0.296
WS_2-$MoSe_2$ heterojunction	0.0855	2.377
WSe_2-$MoSe_2$ heterojunction	0.0157	0.215

3.4 Summary

In summary, enlightened by the intrinsic piezoelectricity of TMDCs based two dimensional monolayer, we have designed and simulated a novel piezoelectric device realized by MoS_2 monolayer based PN junction. Its electromechanical property was simulated by first-principle calculations. 0.31 V of output voltage can be achieved by 0.051 eV/ $Å^3$ of the laterally tensile stress, which leads to 8% strain in transport direction. We have also demonstrated the time domain-output voltage in the case of the applied stress in Sine waveform. The investigation on size-dependent performance demonstrates that by increasing width, length and layer number the output will finally converge to constant output. Our investigation on the doping effect shows that various doping positions affect

slightly on the output voltage and the low concentration gives rise to higher output performance. The piezoelectric performance based on 4 different TMDCs-heterojunction were also simulated. We conclude that the structure with higher EPD can obtain higher output voltage. Our study suggests a novel TMDCs PN junction and heterojunction based mechano-electric generator with high output voltage. This may open up a suite of applications in 2D-TMDCs based piezoelectric transistor.

Chapter 4 Strain engineered Phosphorene nanotube and its applications in field effect transistors

Nowadays, phosphorene, a new 2D material, was prepared successfully in the laboratory and has immediately received considerable considerations. Both experimental and theoretical studies turn out that phosphorene possesses intrinsic bandgap as well as high carrier mobility [81-83] . The electron mobility reaches over 2000 cm2/Vs under room temperature (RT) predicted by theoretical calculation [84,85] . Also, narrow but finite bandgap makes it well-suited for photodetector applications [86]. Thus phosphorene was believed to be a promising candidate for future nanoelectronics. Another attractive feature distinguishing itself from other 2D materials is its profoundly anisotropic electrical conductance along various directions.

During the past decade 1 dimensional (1D) materials have attracted a great deal of attentions among the scientific community. 1D ZnO and GaN nanostructures exhibit numerous electronic and optoelectronic applications such as ultraviolet (UV) laser, field-effect transistor, solar cells, gas sensor, UV photodetector, photo catalyst, light-emitting diode applications and nano power generators. Recently 1D phosphorene nanotube (PNT) was explored theoretically. Previous study showed that the PNT exhibits direct bandgap, which is modified by diameter enlargement. In selected PNTs, a metal-insulator transition

can be induced by strain or by changing the number of walls. In this study we expect that wrapping-engineering on 2D phosphorene, which models 1D phosphorene nanotube (PNT), can also tune the electrical conductance. Single-walled TMD nanotubes (SWTMD NTs) have interesting electronic properties that depend on their diameter and chirality. We explicitly report the electronic properties of armchair PNTs (APNT) in different diameters. The strain and size effect on the bandstructure, the electron and hole effective mass and the carrier mobility are investigated for room temperature. Our study indicates that the compressive strain applied along the transport direction in our 1D structure can abate the direct bandgap as well as improve the carrier mobility. The diameter enlargement can also enhance the electronic conductance. The carrier mobility approaches its saturation value of 2D phosphorene as the diameter enlarges to infinity. Our observed wrapping-engineered high conductance provides many opportunities for novel applications in nano-photodetector, light-emitting diode and field-effect transistor.

4.1 Armchair phosphorene nanotube (APNT)

In this study, first principle calculations were carried out by using the Virtual Nanolab Atomistix ToolKit (ATK) package with density functional theory (DFT). The localized density approximation (LDA) exchange correlation with a double zeta polarized (DZP) basis is used with a mesh cut-off energy of 150 Ry. The electronic temperature is all set to 300 K for our simulations. All atomic positions and lattice constants were optimized by using the generalized gradient approximations (GGA) with the maximum Hellmann-Feynman forces of 0.05 eV/Å, which is sufficient to obtain relaxed structures. The Pulay-

mixer algorithm is employed as iteration control parameter with tolerance value of 10^{-5}. The maximum number of fully self-consistent field (SCF) iteration steps is set to 100.

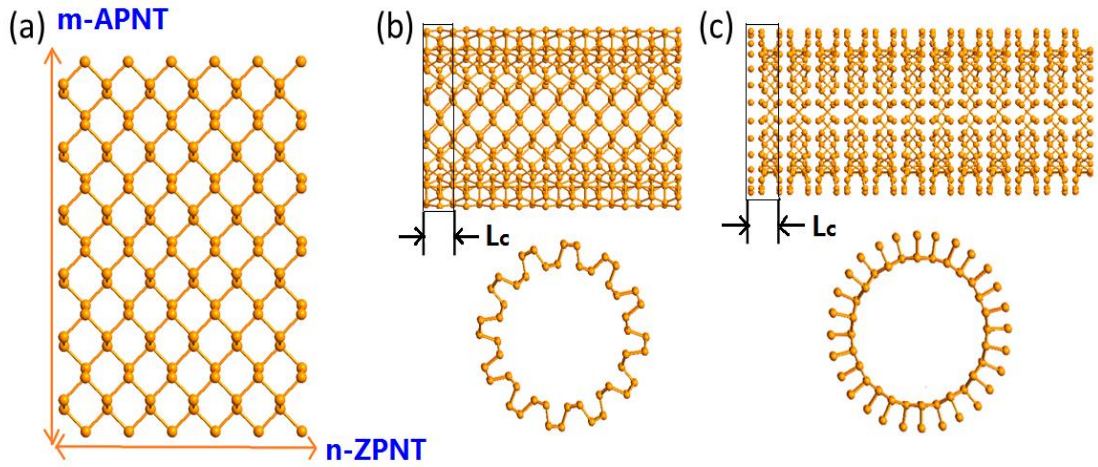

Figure 4.1 The schematic of PNTs: (a) 2D phosphorene nanosheet (b) Side and axial view of the armchair phosphorenen nanotube (APNT). (c) Side and axial view of the zigzag phosphorene nanotube (ZPNT). L_c is the lattice parameter in transport direction.

Single-walled Phosphorene NTs (PNTs) can be classified as armchair nanotubes (ANTs) and zigzag nanotubes (ZNTs) based on their chiral vectors, as displayed in Figure 4.1. In this study we focus on the electronic properties of APNTs. N_a-APNT represents the phosphorene nanotube rolled up by N_a times of unit cells in armchair direction. In this study N_a is varied from 10 to 16 to investigate the size effect on the electronic properties of APNT. The simple orthorhombic box in 60Å × 60Å × L_c size is employed as the sampled system in our investigation, where L_c is the lattice parameter along the transport direction. The periodic boundary conditions were applied for the simple orthorhombic

lattice box, which contains N_a times of unit cells. Each unit cell, also serving as the primitive cell of single layer phosphorene, composes of 4 basic phosphorus atoms. A separation of 60Å for the adjacent nanotubes is employed to minimize the neighboring interaction. We used 1 × 1 × 11 Monkhorst-Pack k-grid mesh in this simulation on our 1D structures. The self-consistent field calculations were checked strictly to guarantee fully converging within the iteration steps.

For the first part of our report, we employ 12-APNT to investigate the strain effect on its electronic properties. The optimized structure is the unit cell with lattice parameter L_c of 3.24 Å.As displayed in Figure 4.1(b), the strain is defined as $\varepsilon = (L - L_c)/L_c$, where L_c and L are equilibrium and strained lattice values in transport direction, respectively. In this study we investigate the structure applied by the strain varied from -5% to 5% with incremental step of 1%.

Firstly we investigate the strain effect on the electronic bandstructure of 12-APNT. The electronic bandstructure of 12-APNT under 0, 5% and -3% were displayed in Fig 4.2, respectively. They all exhibit direction bandgap consisting of CBM and VBM both at Γ-point. In our calculation, all the PNTs are considered as one-dimensional systems, and just K-points along the axial direction are calculated. The bandstructure at the transition between metal and semiconductor was also demonstrated. This transition occurs at high compressive strain ε with value of -10%. The bandgap is reduced by compressive strain whereas increasing monotonically by higher tensile strain. The bandgap for unstrained structure is 0.363eV, which is in fair consistence with 0.56eV by other publication [42]. As opposite regulatory change of bandgap by strain effect on PNTs, tensile strain can

reduce the bandgap of 1D MoS_2 nanotubes and realizes semiconductor to metal transition at the critical value of about 8% strain [43].

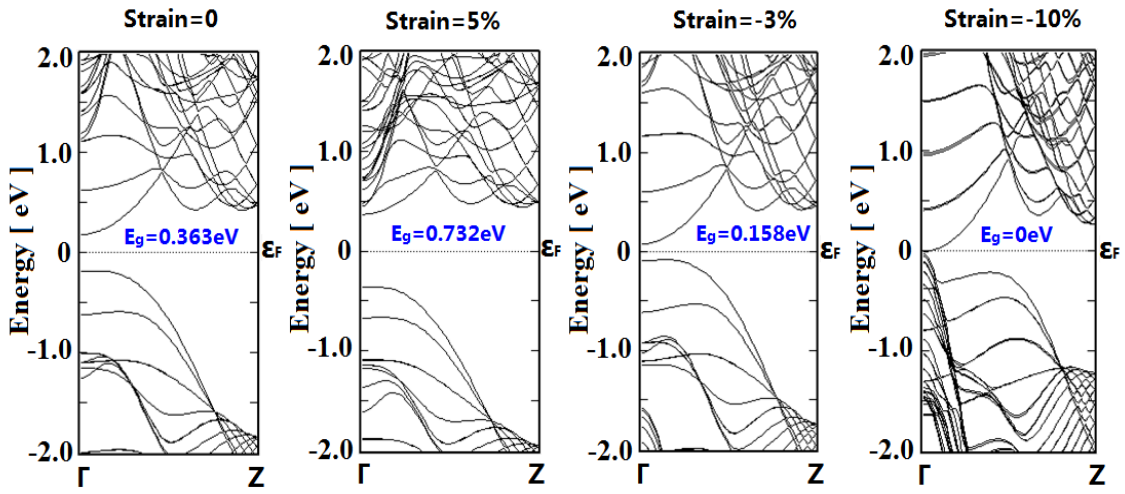

Figure 4.2 The bandstructure of 12-APNT under applied strain of 0, 5%, -3% and -10%, respectively.

Next we considered the total energy of our sampled system as a function of the lattice parameter L_c. As shown in Figure 4.3(a) the most stable system with minimum total energy is at L_c= 3.24 Å. For a 1D crystal, the elastic modulus (stiffness) $C = [\partial E^2/\partial \varepsilon^2]\,/L_c$. The total energy vs. strain relation was fitted by the quadratic parabolic curve: $E = A\varepsilon^2$. Accordingly we got value of 349.92 ev/Å for elastic modulus of 12-APNT by $C = \frac{1}{Lc} dE^2_{total}/d\varepsilon^2 = 2A/L_c$. This is much higher than value of 179.21 ev/Å for

(10, 0) zigzag MoS_2 nanotube [43], signifying much stiffer resistance to the applied strain, as well as implying a higher carrier mobility along the transport direction.

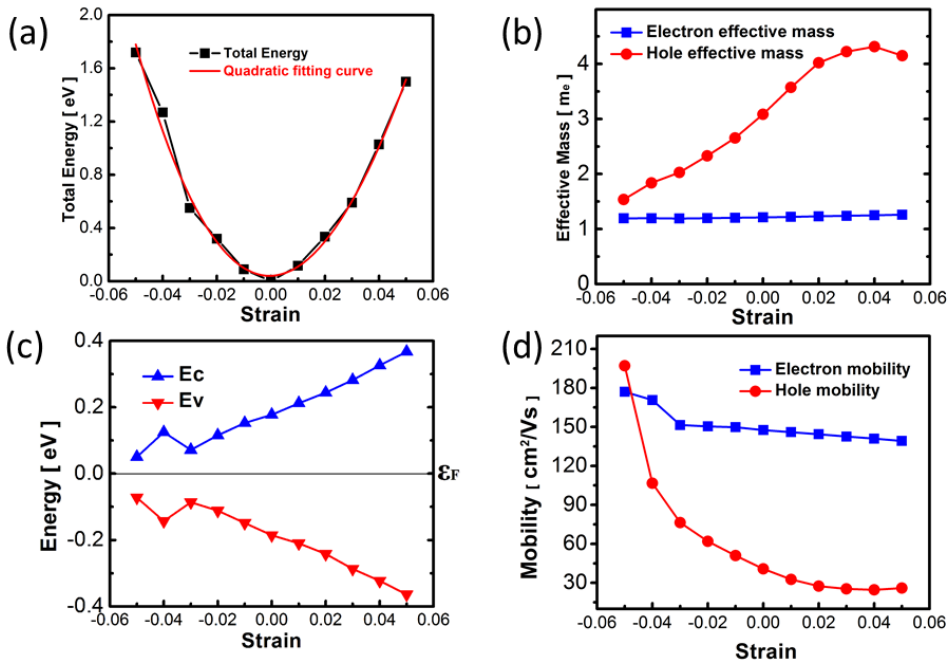

Figure 4.3 The mechanic and electric properties of 12-APNT under applied strain from -5% to 5%. (a) The total energy vs. strain. (b) The electron and hole effective mass vs. strain. (c) The conduction band minimum (CBM) and valence band maximum (VBM) vs. strain. (d) The carrier mobility vs. strain

Besides the bandgap and the total energy, strain also changes the energy band curvature which is directly related to the carrier effective mass (m^*): $m^* = \hbar^2/(\partial^2 E/\partial k^2)$, where ħ is the reduced Planck constant, E is the energy and k is momentum. In this study, since CBM and VBM are keeping at Γ(0, 0) in the Brillouin zone for the various

strained and enlarged structures, we focus on the electron and hole effective mass at Γ(0, 0). Figure 4.3(b) displayed the evolution of carrier effective mass with respect to the various strain. Due to the intrinsic 1D structure, the effective mass is only evaluated along the transport direction. The electron and hole effective mass are 1.21m_e and 3.08m_e for unstrained structure. The hole effective mass m_h^* is more sensitive to the strain than the electron effective mass m_e^*. m_e^* is slightly enhanced from 1.19 m_e to 1.26 m_e under strain in a large variety of -5% to 5%. whereas $m_h^*$is increasing monotonically up to 4% strain, then undergoing slight reduction for 5% strain. R.X. Fei *et al.* reported that the electron effective mass of 2D phosphorene monolayer is 1.246 m_e along the zigzag direction [90], which is very close to that of our wrapping structure. Zigzag direction is equivalent to the transport direction in 1D APNT. Our study reveals that the wrapping-engineering has a limited effect on the electron effective mass of phosphorene. The evolution of the conduction band minimum (CBM) and valence band maximum (VBM) with respect to strain are displayed in Figure 4.3(c). They varied linearly with regard to the strain within the range from -3% to 5%. Thus the deformation potential (DP), which is defined as the shift rate of band edge with respect to strain: $dE_{edge}/d\varepsilon$, is keeping constant within this region. We got the value of 3.78 eV and 3.51 eV for the DP constant of electrons and holes, which will be used for the calculation of carrier mobility.

The carrier mobility is a very important parameter to evaluate the electrical properties of materials. Since the carrier effective mass is affected by tensile strain, it is expected that the carrier mobility will also be affected. K. Kaasbjerg *et al*. have clearly shown that the carrier mobility in these 2D monolayers is dominated by acoustic phonon

scattering via intra and intervalley deformation potential couplings at room temperature [18,19]. The mobility can be figured out by the deformation potential (DP) theory raised by Bardeen and Shockley [44]. Based on the effective mass approximation, the DP theory determines the carrier mobility of 1D system as [45]:

$$\mu_{1D} = \frac{e\hbar^2 C}{(2\pi K_B T)^{1/2} |m^*|^{3/2} {E_1}^2} \quad (1)$$

where e is electron charge, m* is the carrier effective mass, K_B is the Boltzmann constant and T is the temperature, E_1 is the DP constant denoting the shift of the band edges (E_{edge}) (CBM for electrons and VBM for holes) induced by strain (ε): $dE_{edge}/d\varepsilon$. As aforementioned C=349.92ev/ Å, signifying the elastic modulus of a uniformly deformed crystal activated by the strain. Figure 4.3(d) shows the variation of carrier mobility with response to the strain applied along the transport direction. Both electron mobility and hole mobility slightly decrease with the larger tensile strain. The hole mobility is more sensitive to the tensile strain than electron mobility. As demonstrated the hole mobility reduces from 40.7 cm^2/Vs to 26.0 cm^2/Vs when the strain is reaching 5%. This is mainly attributed to the elevated hole effective mass induced by the tensile strain. The compressive strain gives rise to much more dramatic influence on carrier mobility, especially for the strain within the range：-3% ≤ ε ≤ -5%. The hole mobility are boosted sharply by 4.8 times from 40.7 cm^2/Vs to 197.0 cm^2/Vs as the compressive strain increases to -5%. This dramatic enhancement benefits from the significantly reduced DP constant caused by larger strain. As aforementioned the DP constants for both electrons and holes are remaining constant value during the strain from -3% to 5%, hence the main factor for the slightly reduced mobility is the enhanced carrier effective mass. Our study suggests the elevated mobility

of 1D structure activated by compressive strain, which is differing in the strain effect on MoS_2 monolayer: the carrier mobility are significantly enhanced by tensile strain [26].

The carrier mobility of 1D nanotubes is associated with deformation potential constant, the elastic modulus, temperature and electron and hole effective mass. In this study the temperatures are all set to 300K that we only consider all the simulations and calculations at room temperature. Firstly we begin with the bandstructure of APNT with N_a varied from 10 to 16. The bandgap transition, the elastic modulus, deformation potential as well as carrier effective mass are discussed in sequence. The evolution of carrier mobility with regard to N_a is calculated by DP theory, revealing the significant improved mobility motivated by enlarged size of APNT.

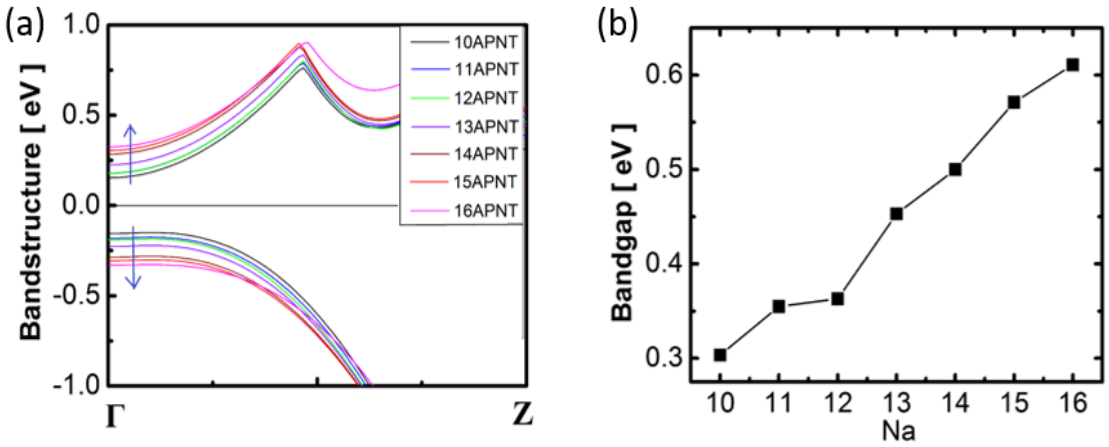

Figure 4.4 (a) The transition of bandstructure of APNT for various Na ($10 \leq Na \leq 16$). (b) The evolution of bandgap vs. N_a.

N_a-depended bandstructure is demonstrated in Figure 4.4(a). All the structures are fully optimized to the most stable system at first step. The valence band (VB) and conduction band (CB) are shifted oppositely to each other, leaving a larger bandgap by enlarged APNT diameter. Figure 4.4(b) exhibits the direct bandgap at Γ-point as a function of N_a. As shown the bandgap of 10-APNT is 0.304 eV, while increasing to 0.611 eV for 16-APNT. The energy band spectra of single-walled PNTs should approach to that of 2D monolayer counterpart, when the diameter increases to infinity. Also, the infinite 2D phosphorene exhibits direct bandgap about 0.9 eV at Γ-point [90], which is expected to be the limit value of the phosphorene nanotube with infinitely enlarged diameter. The narrow and direct bandgap make APNTs well-suited for applications in infrared detectors.

Next we investigate the mechanic property of 1D APNTs with various diameters. As demonstrated in Figure 4.5(a), the elastic modulus (C) is monotonically enhanced with diameter enlargement, indicating much stiffer structure with the diameter enlargement. It increases from 309.3 eV/Å for 10-APNT to 516.7 eV/Å for 16-APNT. As aforementioned C of PNTs is significantly higher than that of MoS_2 nanotube, which is favored for realizing high carrier mobility along the transport direction. The optimized lattice parameter L_c along the transport direction for relaxed structures are also shown. L_c is increasing initially by N_a up to 12, then keeping constant value of 3.24 Å for further

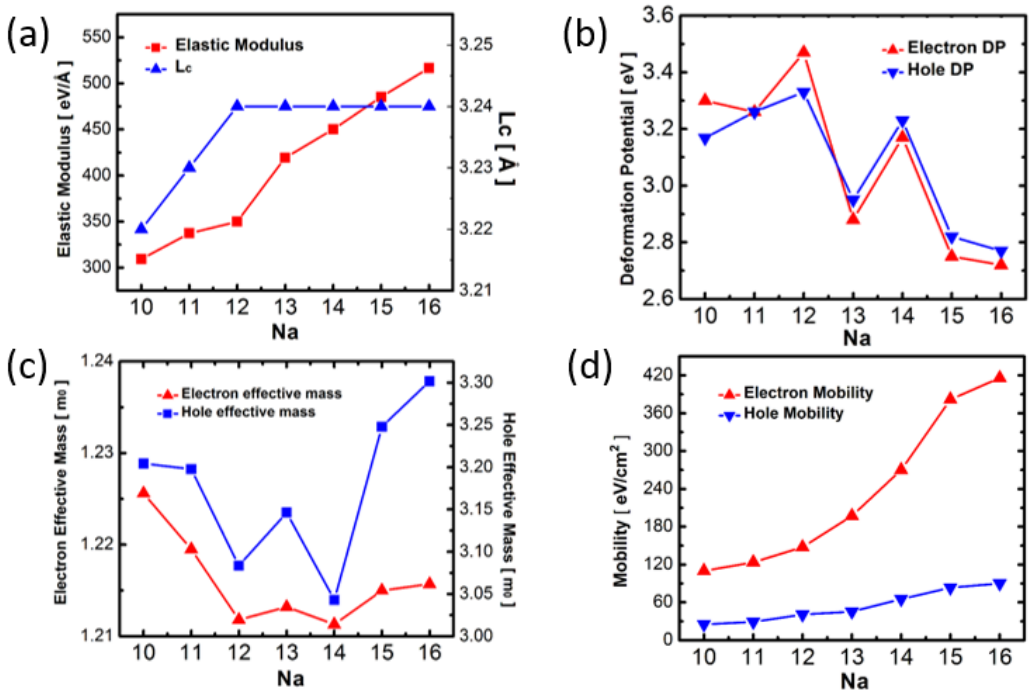

Figure 4.5 The mechanic and electric proeperties of APNTs vs. Na ($10 \leq N_a \leq 16$). (a) The elastic modulus C and lattice parameter L_c vs. N_a. (b) The deformation potential constant of electrons and holes vs. N_a. (c) The electron and hole effective mass vs. N_a. (d) The carrier mobility vs. N_a.

enlargement. This is smaller compared to 3.35 Å of the relaxed 2D monolayer, indicating that 1D wrapping engineering compresses the lattice in transport direction. The DP constant of electrons and holes are displayed in Figure 4.5(b). They are irregularly tuned within the range from 2.72 eV to 3.47 eV for electrons and from 2.77 eV to 3.33 eV for holes by the enlarged diameter. They exhibit much lower electron DP constant than that of MoS_2 nanotubes (7.0-9.5 eV), which is expected to induce much higher electron mobility in APNTs.

The carrier effective mass are also investigated for APNTs with various diameters. As displayed in Figure 4.5(c), the electron mobility is fluctuated within small range (1.210 m_e-1.226 m_e) for $10 \leq N_a \leq 16$. Also the hole effective mass is oscillating more sensitively (3.04 m_e-3.30 m_e) to the diameter enlargement. The evolution of the electron and hole mobility as a function of N_a is displayed in Figure 4.5(d): they are both enhanced with the diameter enlargement. The electrons with high mobility of 109.9 cm^2/Vs to 415.7 cm^2/Vs for $10 \leq N_a \leq 16$ dominate the charge transport. The hole mobility increases from 25.2 cm^2/Vs to 90.1 cm^2/Vs with the diameter enlargement. As the diameter enlarges to infinity, the carrier mobility are expected to saturate to that of infinite 2D phosphorene, which possesses 2000 cm^2/eV of electron mobility.

We have explicitly explored the various electric properties of 1D phosphorene nanotube by first-principle simulations. The intrinsic semiconducting behavior is exhibited along the transport direction for APNTs. The investigation of strain effect on 12-APNT reveals that the bandgap is reduced by compressive strain. Also, the calculation by using deformation potential theory indicates that the compressive strain can induce higher carrier mobility. Moreover, the study on size effect shows that the carrier mobility are significantly improved by the diameter enlargement. And, the electron mobility is much higher than that of holes, indicating a dominant charger carrier for electric conductance. Overall, the moderate direct bandgap and the high carrier mobility of 1D phsphorene nanotube renders it a promising potential used for future filed-effect transistors as well as in photodetectors. The method and conclusion developed in this work can also benefit the research on other nano 1D and 2D materials and devices.

4.2 Zigzag Phosphorene nanotube (ZPNT)

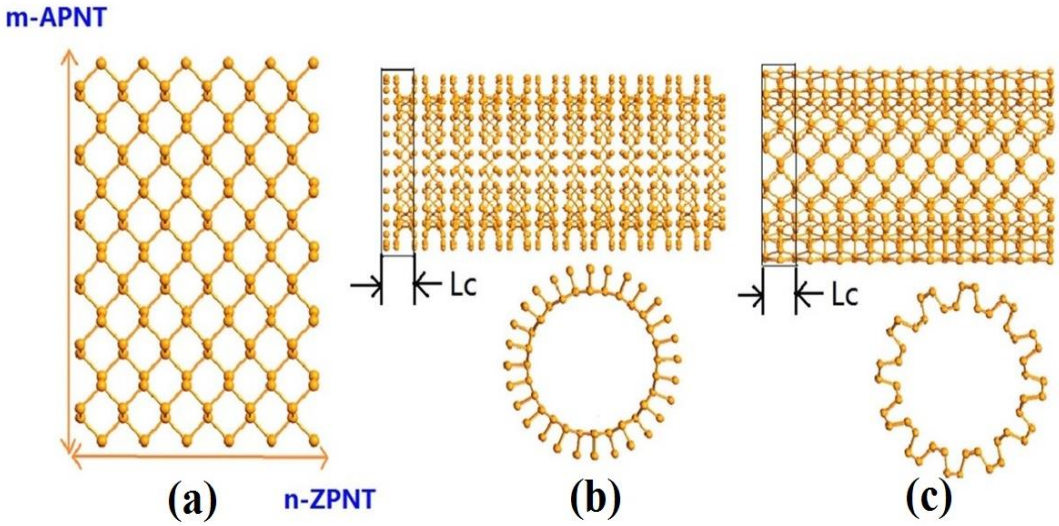

Figure 4.6 The schematic of PNTs: (a) 2D phosphorene nanosheet and (b) side and axial view of the zigzag phosphorene nanotube (ZPNT). (c) Side and axial view of the armchair phosphorene nanotube (APNT). L_c is the lattice parameter in transport direction.

I propose the strain engineered Dirac Fermions in zigzag PNTs (ZPNTs) by first principle calculations. We demonstrate that Dirac cones emerge at lattice parameter (L_c) within a wide range. The investigation on the density of states (DOS) indicates that the Dirac cone mainly stems from p shell of phosphorus atoms. The characterization of 12-ZPNTs based field effect transistor (FET) provides a strong evidence on the semimetal property of 12-ZPNT at L_c of 4.10Å, due to the observed weakly modulated drain-source current by gate voltage, while it demonstrates semiconducting property at L_c of

4.6 Å. Our study suggests a novel 1D material possessing Dirac Fermions with high transport motivation via axial strain, offering many opportunities for future applications in high conductance devices.

In this study, first principle calculations were carried out by using the Virtual Nanolab Atomistix ToolKit (ATK) package with the density functional theory (DFT) [92]. The localized density approximation (LDA) exchange correlation with a double zeta polarized (DZP) basis was used with a mesh cut-off energy of 150 Ry.[43] The electronic temperature was all set to 300 K. All the atomic positions and lattice parameters were optimized by using the generalized gradient approximations (GGA) with the maximum Hellmann-Feynman forces of 0.05 eV/ Å, which is sufficient to obtain relaxed structures [43]. The Pulay-mixer algorithm was employed as iteration control parameter with tolerance value of 10^5 [93]. The maximum number of fully self-consistent field (SCF) iteration steps was set to 100 [43]. For the calculations on the current-voltage characterization of ZPNT FETs, we extended the number of SCF iteration steps to 1000, which is sufficient for the device-related simulations [43]. In the transport direction Dirichlet boundary condition was applied on the two opposite electrodes, in which the electric potential was held homogeneously across the boundary [94]. Neumann condition was employed on the other two directions, in which the electric field was held homogeneously at the boundary [94]. The self-consistent field calculations were checked strictly to guarantee fully converging within the iteration steps.

Single-walled PNTs can be classified as zigzag nanotubes (ZPNTs) and armchair nanotubes (APNTs) based on their chiral vectors, as shown in Fig. 4.6. N_a-ZPNT indicates the nanotube size: the nanotube is rolled up from its nanoribbon counterpart with width of N_a times of unit cells in zigzag direction. N_a was selected from 12 to 16 to investigate the size effect on the electronic properties of ZPNTs. The simple orthorhombic box in 60Å × 60Å × L_c size was employed as the sampled region in our investigation, where L_c is the lattice parameter along the transport direction. The sampled region is enclosed within the solid lines as shown in Fig. 4.6(b). Periodical boundary conditions have been applied for the sampled region in simple orthorhombic lattice, which contains N_a unit cells [95]. Each unit cell, which also serves as the primitive cell of single layer phosphorene, composes of 4 basic phosphorus atoms. A separation of 60 Å for the adjacent nanotubes was employed to minimize the mirroring interaction. We used 1×1×11 Monkhorst-Pack k-grid mesh on our 1D structures.[44] The self-consistent field calculations were checked strictly to guarantee fully converging within the iteration steps. For the calculations on the source-drain current of devices, the non-equilibrium Greens function (NEGF) was employed:

$$I = \frac{2q}{h} \int dE.T(E)\{ f_L(\mathrm{E}, \mu_L) - f_R(\mathrm{E}, \mu_R)\} \quad (1)$$

where factor 2 counts for spin degeneracy, q is electrical charge of carrier, h is Planck's constant, T (E) is transmission spectrum coefficient, $\mu_{L(R)}$ is chemical potential of left (right) electrodes and $f_{L(R)}$ is the Fermi distribution of left (right) electrode.

For the first part of our study, we investigate the electronic bandstructure at different lattice parameters. Firstly, the evolution of the total energy of the unit cell in

12-ZPNT with different lattice parameters L_c is investigated, as shown in Fig. 4.6(a). It reaches minimum at L_c of 3.85Å, indicating the intrinsic lattice parameter for 12-ZPNT.

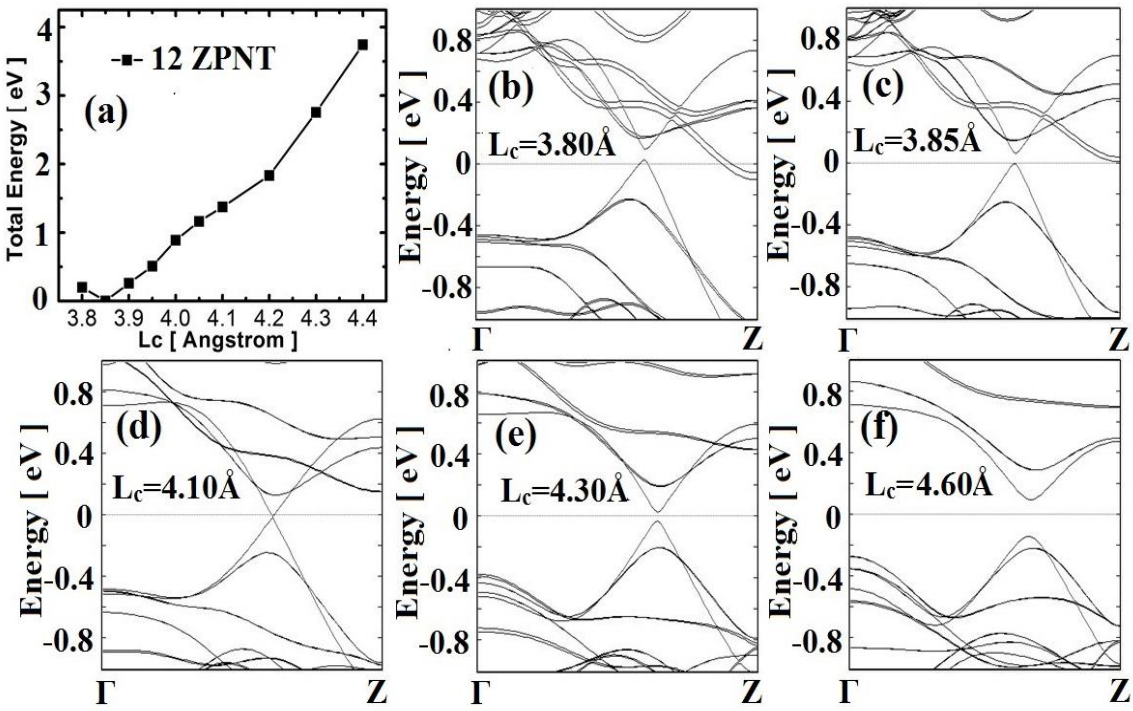

Figure 4.7 (a) the total energy vs. Lc for 12-ZPNT. The bandstructure of 12-ZPNT at (b) L_c=3.80 Å; (c) L_c=3.85 Å; (d) L_c=4.10Å; (e) L_c=4.30 Å; (f) L_c=4.60 Å, respectively. The Fermi level is set to energy=0.

Fig. 4.7(b)-(f) show the electronic bandstructure of the structure with L_c of 3.80Å, 3.85Å, 4.10Å, 4.30Å and 4.60Å, respectively. In our calculation, all ZPNTs were considered as one-dimensional systems, therefore, only K-points along the axial direction were calculated. It is noteworthy that 12-ZPNT undergoes phase transition from metal

to semimetal and from semimetal to semiconductor, respectively. Extraordinarily, the semimetal property is exhibited distinctly by different L_c: valence band maximum

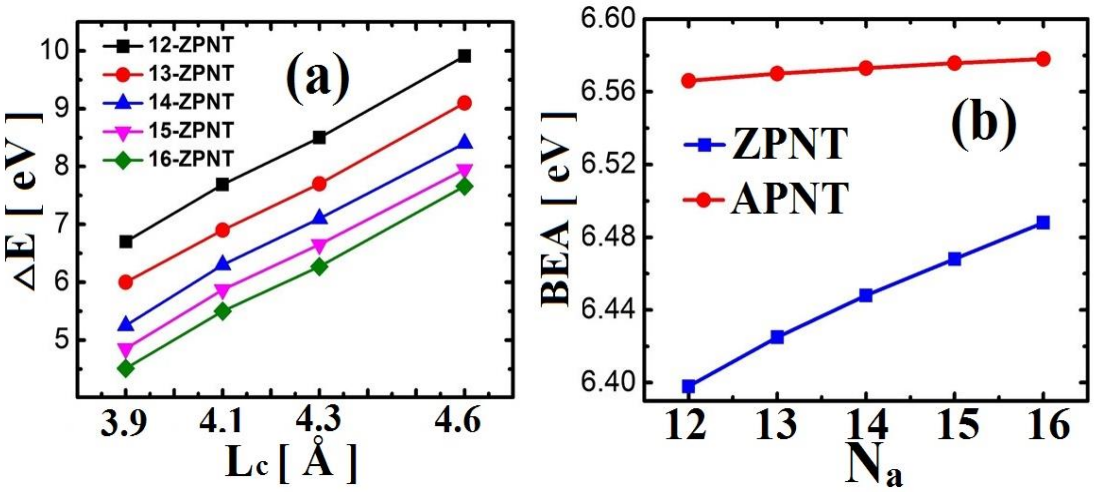

Figure 4.8 (a) The wrapping energy as a function of Lc for Na-ZPNT. Na is varied from 12 to 16. (b) The comparison of the binding energy per atom (BEA) between ZPNT and APNT.

(VBM) and conduction band minimum (CBM) are located at different positons in Brillouin zone at L_c of 3.85Å, while they are converging at the cross point at [0, 0, 0.333] in k-space at L_c of 4.10Å. With further increasing L_c, the structure exhibits semiconducting property along the transport direction: it opens up a direct bandgap of 0.24eV at [0, 0, 0.333] at L_c of 4.60Å. Our investigation suggest the bandstructure of ZPNTs with phase transitions, indicating different electronic properties at different lattice parameters tuned by strain.

Next we turn to investigate the structural stability of ZPNTs. Fig. 4.8(a) shows the wrapping energy as a function of the nanotube diameter. The wrapping energy is denoted by the difference between the total energy of the unit cell in zigzag phosphorus nanotube (ZPNT) in comparison with that of its counterpart in zigzag phosphorene nanoribbon (ZPNB). As demonstrated among our selected N_a, 12-ZPNT has the highest wrapping energy while it is lowest for 16-ZPNT. This indicates that the larger diameter of ZPNT, the higher stability of the structure. This is due to the smaller curvature at the

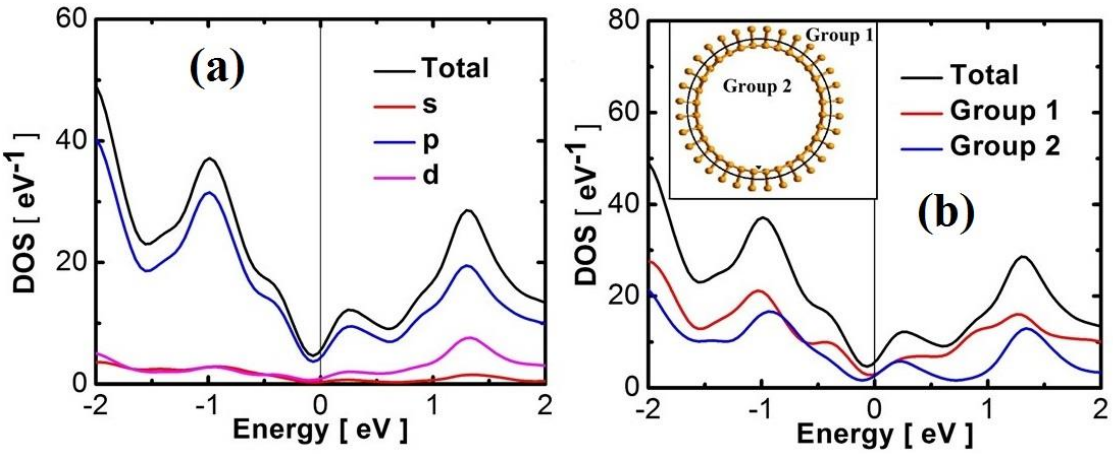

Figure 4.9 The analysis of the density of states (DOS) of 12-ZPNT: (a) The total DOS and separated DOS by s, p and d atomic shell, respectively. (b). The total DOS and separated DOS by group 1 and group 2.

nanotube surface that requires lower wrapping energy for ZPNT with larger diameter. Also, we investigated the binding energy per atom (BEA), which can directly be related to the major stability of nanotube structures. Fernández et al. [96] proposed the following formula to calculate BEA values:

$$BEA = (nE_{atom} - E_n)/n \quad (2)$$

where E_{atom} is the total energy of single P atom and E_n is the total energy of n atoms included in the unit cell. We used this formula to calculate BEA for ZPNTs with different diameters. The stability of armchair PNTs (APNTs) was also evaluated by BEA. Generally APNTs exhibit higher BEA than ZPNTs, indicating the higher structural stability. Also, BEA increases with the larger diameter, both for ZPNTs and APNTs. This reveals that the stability was improved for nanotube structures with larger diameter and smaller surface curvature. This suggestion is consistent with the evaluation from the perspective of the wrapping energy.

We further analyze the physical origin of the unique Dirac cone. Fig. 4.9(a) shows the density of states (DOS) of 12-ZPNT at L_c of 4.00Å. As demonstrated the density of states around Fermi level majorly stem from p orbital shell of phosphorus atom. To further consider the origin of the Dirac cone, we classified the phosphorus atoms into two groups: the atoms at outer-ring noted as group 1 and the atoms at inner-ring marked as group 2, which was depicted in the inset of Fig. 4.9(b). Fig. 4.9(b) displayed the DOS of these two groups, respectively. It indicates that in comparison with group 1, group 2 atoms make larger contribution to the Dirac cones.

4.3 PNT based transistors

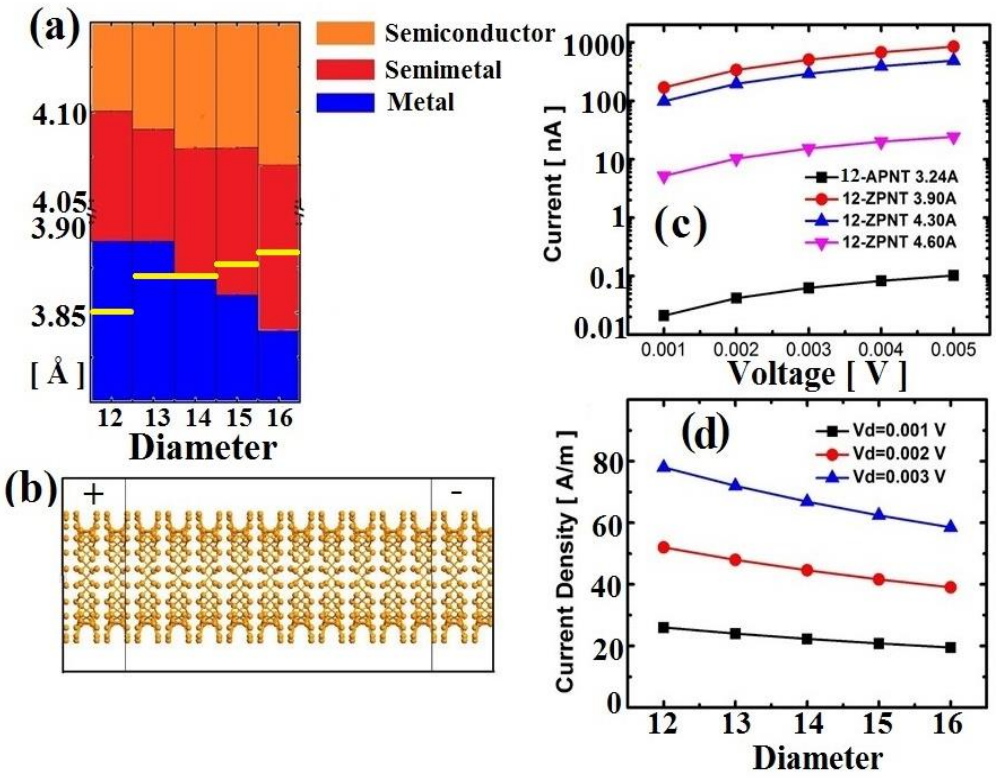

Figure 4.10 The current-voltage characteristic of ZPNT based transistor: (a) The profile of phases transition and distribution by L_c for N_a-ZPNT for N_a varied from 12 to 16. Yellow line represent the intrinsic L_c for each N_a-ZPNT. (b) The schematic of ZPNT based transistor. (c) Current vs. bias voltage for 12-ZPNT at 3.90Å, 4.30Å, 4.60Å and 12-APNT at 3.24Å, respectively. (d) The current density vs. ZPNT diameter at bias voltage of 0.001V, 0.002V and 0.003v, respectively.

The phase transition for ZPNTs with different diameters are investigated. Fig. 4.10(a) shows the profile of the phase transitions of N_a-ZPNTs with different diameters by N_a varied from 12 to 16. L_c corresponding to the transition boundary, both from metal to semimetal and from semimetal to semiconductor, are gradually reduced as the larger nanotube diameter. However, the intrinsic lattice parameter, which is leading to

the minimum total energy of the unit cell, gradually increases as the larger diameter. As expected, due to the smaller curvature of ZPNT with larger diameter, the lattice becomes relaxed so as to release itself in the transport direction, leading to the increased L_c. As N_a becomes very large, i.e., the diameter increases to infinite, L_c should approach to that of its 2D monolayer counterpart. In addition, 2D phosphorene exhibits intrinsic L_c of 4.62Å at transport direction, which is expected to be the limit value for ZPNT with very large N_a. It is noteworthy that 12-ZPNT and 13-ZPNT intrinsically exhibit the metallic property, while 15- and 16-ZPNT demonstrate the semi-metallic property along the transport direction. The phase profile indicates that the conductance of nanotubes reduces monotonically under the tensile strain. This suggestion is evidenced by the calculations on the current-voltage characterization of nanotube transistor (Fig. 4.10(c)). The schematic of 12-ZPNT based transistor is displayed in Fig. 4.10(b). Generally the current reduces significantly as the increasing L_c, and it increases proportionally to the higher bias voltage within the small range from 0v to 0.005V. We also give a comparison between the electrical performance of 12-ZPNT and 12-APNT. Our previous study indicated that APNTs exhibit strain-modulated semiconducting property. The calculation results shown in Fig. 4.10(c) attest this characterization: the semi-metallic 12-ZPNT has much higher conductance in several orders of magnitude than that of 12-APNT with semiconducting property. Moreover, it appears noteworthy that the phase transition boundaries reduce as the larger ZPNT diameter, implying that the conductance of ZPNTs decreases with the diameter enlargement. This is further

evidenced by the calculations shown in Fig. 4.10(d): the current smoothly reduces under the same bias voltage for the nanotube with the larger diameter.

The ZPNT based field effect transistors (ZPNT-FETs) have also been investigated by adding cylinder metal gate around the nanotube, the schematic of which is shown in Fig. 4.11(a). We employed pn junction as the channel for ZPNT-FETs: silicon atom replaces the phosphorus at the left side to realize p-type doping while sulfur

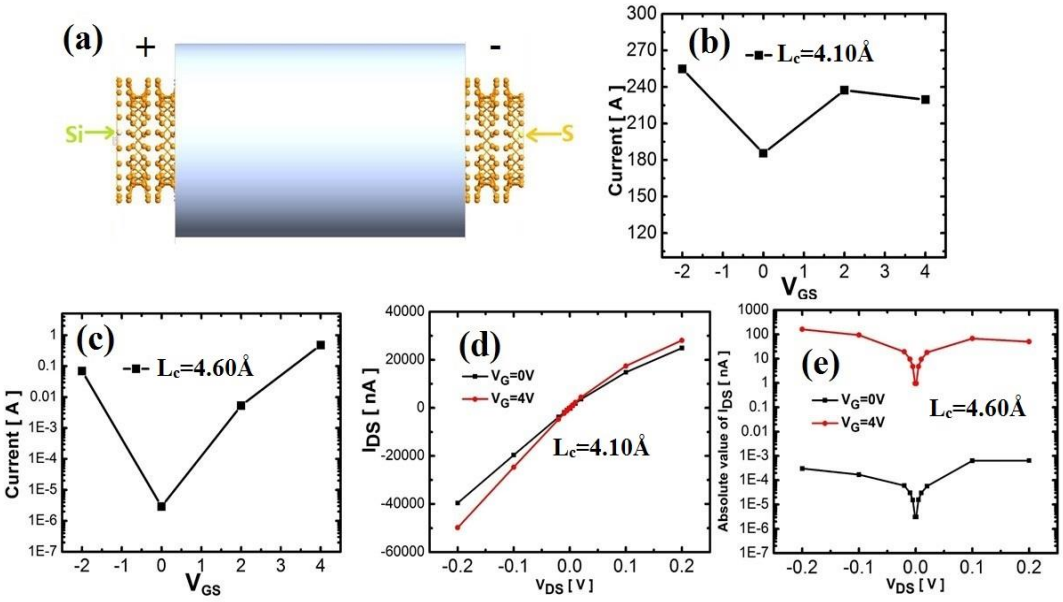

Figure 4.11 The characterization of 12-ZPNT field effect transistor (FET) based on pn junction. (a) The schematic of 12-ZPNT FET. Si replace P to realize p-type doping at left side. S replace P to realize n-type doping at right side The metal tube gate was added around ZPNT. Drain-source current (I_{DS}) vs. Gate votage (V_{GS}) for 12-ZPNT FET at (b) L_c= 4.10Å; (c) L_c= 4.60Å. Drain-source current (I_{DS}) vs. bias voltage (V_{DS}) at (d) L_c= 4.10Å; (e) L_c= 4.60Å.

substitutes phosphorus to achieve n-type doping at right side in the channel. The device with L_c of 4.10Å and 4.60Å along the transport direction were separately investigated by a variety of the gate voltage at -2V, 0V, 2V and 4V, respectively. As aforementioned, the structure with L_c of 4.10Å exhibits semi-metallic property while it demonstrates semiconducting transport at L_c of 4.60Å. Our calculations on the behavior of ZPNT FETs attest this suggestion. Fig. 4.11(b) demonstrates the gate voltage tuned drain source current (I_{DS}) for the device at L_c of 4.10Å. I_{DS} does not improve significantly under the modulation of gate voltage. Fig. 4.11(c) shows the semiconducting transport of 12-ZPNT FET with L_c of 4.60Å. The on/off ratio is obtained in excess of 10^5 at V_{DS}=0.001v. It is noteworthy that the on current is obtained to ~1nA under V_{GS}=4V, which is significantly smaller in several orders of magnitude than that of 12-ZPNT FET with L_c of 4.10Å. Moreover, we extended the range of V_{DS} to -0.2V to 0.2V to compare I_{DS} vs. V_{DS} for these two devices with distinct L_c. The calculation results are demonstrated in Fig. 4.11(d) and Fig. 4.11(e). I_{DS} increases monotonically, but not strictly proportionally, to the increased V_{DS} for semimetal transport at L_c of 4.10Å. V_{GS} does not modulate I_{DS} effectively. However, in the case of L_c=4.60Å, I_{DS} is going to saturate when V_{DS} is increasing over 0.1V. The on/off is over 10^5 at V_{GS}=4V, indicating an effective metal gate modulation.

4.4 Conclusion

The various electric properties of 1D phosphorene nanotube was explored by first-principle simulations. The intrinsic semiconducting behavior is exhibited along the

transport direction for APNTs. The investigation of strain effect on 12-APNT reveals that the bandgap is reduced by compressive strain. Also, the calculation by using deformation potential theory indicates that the compressive strain can induce higher carrier mobility. Moreover, the study on size effect shows that the carrier mobility are significantly improved by the diameter enlargement. And, the electron mobility is much higher than that of holes, indicating a dominant charger carrier for electric conductance.

We also demonstrated the zigzag phosphorene nanotubes: its strain engineered phase transition and electronic properties. Dirac fermions emerge at the electronic bandstructure during the wide range of lattice parameter at the transport direction. The calculations on the wrapping energy indicate that ZPNT with the larger diameter possesses higher stability. The characterization of current and voltage relation demonstrates that the conductance becomes lower as the higher diameter of ZPNT. Also, as expectation the conductance of ZPNTs is much higher than that of APNTs. Furthermore, we add the metal tube gate to investigate the gate control effect on the pn junction based ZPNT field effect transistors. It is evidenced that 12-ZPNT with L_c of 4.10Å exhibits semimetal property due to the observed weakly tuned gate effect. However, it indicates strong semiconducting transport because 12-ZPNT with L_c of 4.60Å has very effective gate control. Our findings offer extraordinary opportunities for development of high-performance strain-tuned electronic devices based on 1D Dirac materials.

Chapter 5 Strain effect introduced by dielectric layer/2D TMDCs interface

Metal-oxide-semiconductor field-effect transistors (MOSFETs) have shown impressive performance improvements over the past 10 years by incorporating strained silicon (Si) technology. This review gives an overview of the impact of strain on carrier mobility in Si n- and pMOSFETs by considering strain-induced band splitting, band warping and consequent carrier repopulation, and altered conductivity effective mass and scattering rate. Different surface orientations, channel directions, and gate electric fields are included for a fully theoretical understanding. The results are used to predict strain-enhanced silicon-on-insulator (SOI) and multigate device performance, mainly focusing on potential 22-nm and beyond device options such as double-gate and trigate fin field-effect transistor (FinFET) structures. Insights into strain-enhanced potential future channel materials (SiGe, Ge, and GaAs) are also summarized. Finally, recent technology nodes with strain engineering are reviewed, and the future developing trend is given.

Metal/semiconductor contact can induce strain effect are widely reported. The strain effect introduced by Ag and heating effect introduced by Ti to monolayer MoS_2 are also revealed by Raman spectroscopy. However, little is explored on the strain effect induced by dielectric layer/2D TMDCs semiconductor. The quasi-superlattice method was employed. The evolution of separation between Al_2O_3 and MoS_2 monolayer vs. the various

thickness of dielectric layer have been studied. Also the intrinsic lattice parameter of the interface was specified by figure out the minimum total energy. The systematic bandstructure and density of states are explored by various thickness of dielectric layer.

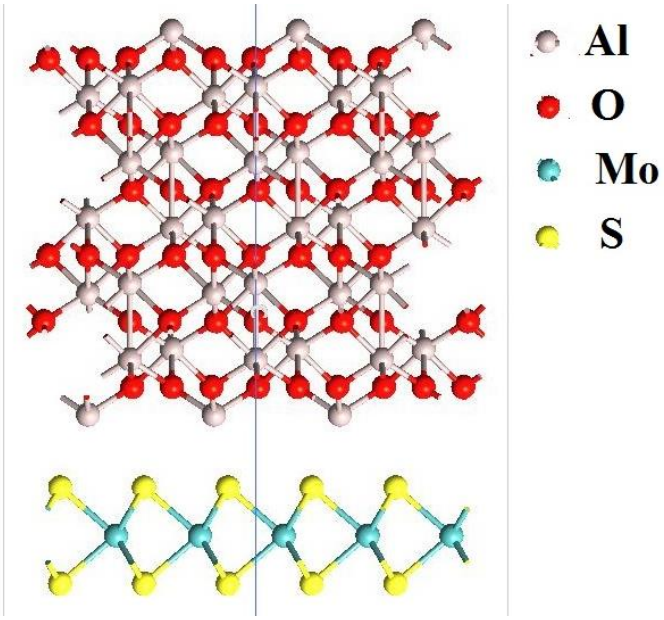

Figure 5.1 Schematic of interface between Al_2O_3 with MoS_2 monolayer

Figure 5.1 displays the schematic of Al_2O_3/MoS_2 monolayer interface. The thickness of Al2O3 dielectric layer is varied at 1.3nm, 2.6nm, 3.9nm and 5.2nm. Firstly, we focus on the thickness of dielectric layer into 1.3nm. The distance between the dielectric layer and MoS2 monolayer is continuously varied from 2.3Å to 2.7Å. Figure 5.2(a) demonstrates the evolution of the total energy of the unit cell as a function of separation distance. It indicates the most stable structure occurs at separation of 2.4Å. Next

step is to investigate the intrinsic lattice parameter of the unit cell. Figure 5(b) demonstrates the total energy of the unit cell vs. the lattice parameter. The total energy reaches minimum at Lc of 9.51Å. Thus the strain induced by dielectric layer with 1.3nm thickness is calculated to be 0.3%.

We also investigate the strain effect in cases of different thickness of dielectric layer. Figure 5.3(a) demonstrates the separation distance between these 2 layers with different thickness of dielectric layer. It indicates that L_c monotonically decreases with increasing thickness. Also I study the intrinsic lattice parameter in cases of different thickness.

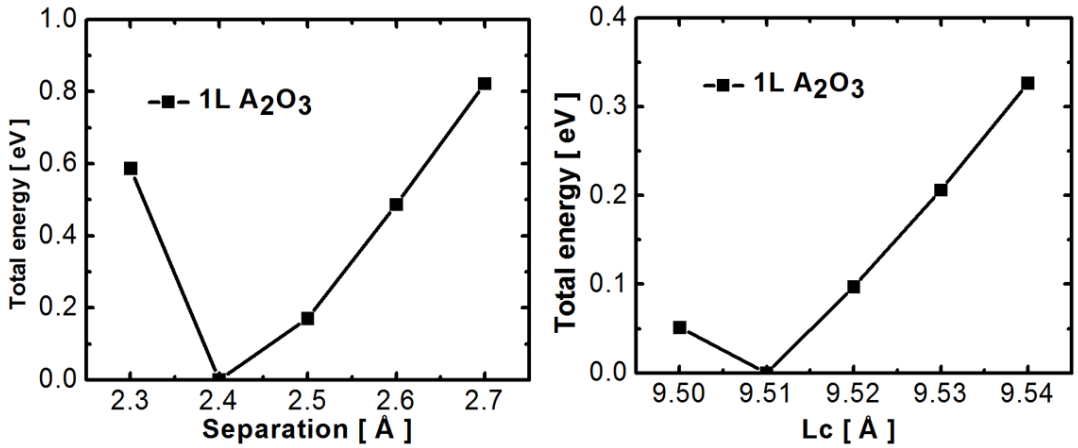

Figure 5.2 The total energy vs. Separation between two layers and the total energy vs. lattice parameter.

The intrinsic L_c at thickness of at 1.3nm, 2.6nm, 3.9nm and 5.2nm is shown to be 9.51Å, 9.52Å, 9.53Å and 9.54Å, respectively. As expectation the intrinsic L_c goes to approach the limit value of 9.594Å, which is the intrinsic Lc of bulk Al_2O_3.

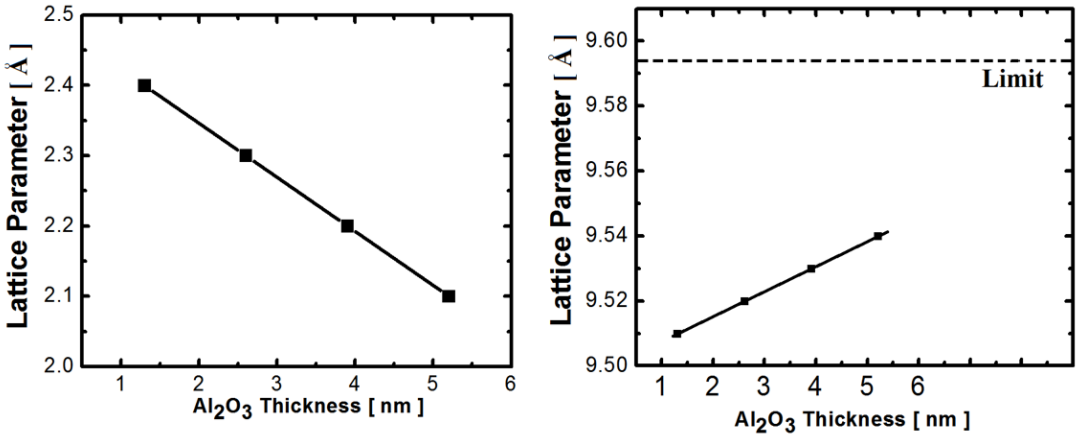

Figure 5.3 The separation between two layers vs. Al2O3 thickness and the intrinsic lattice parameter vs. Al2O3 thickness.

Chapter 6 Future Work

The electrical performance tuned by applied strained is in further investigation. The tensile/compressive strain must have distinct effect on the electrical performance. Also the strain intensity is another factor that determines the electrical performance. Generally, tensile strain improves the output current significantly at two main factors: strain-enhanced carrier mobility and strain-induced higher carrier concentration. In ballistic transport, which require the short channel length usually less than 20nm, constrain the carrier concentration in the channel. Thus the key factor is enhanced carrier mobility induced by strain. Therefore based on the study on the carrier mobility vs. strain, we can further investigate the output current vs. strain.

The next issue is to investigate the strain induced by dielectric layer and electrode metal. In the simulation, the dielectric layer usually requires the lattice matching between dielectric layer and 2D semiconductor channel. The slight mismatching between the lattice of these two layers gives rise to the strain on the channel material. The various channel material (MoS_2, $MoSe_2$, $MoTe_2$, WS_2, WSe_2, WTe_2, ReS_2, PdS_2 and NiS_2) vs. various dielectric material (SiO_2, ZrO_2, Al_2O_3, HfO_2) are in further investigation. The different lattice type between the dielectric layer and TMDCs is the main difficulty in this study. The other method rather than the quasi-superlattice should be proposed to solve this difficulty.

During the last decade, one-dimensional (1D) materials have attracted a great deal of attentions among the scientific community. For example, ZnO and GaN 1D nanostructures exhibit numerous electronic and optoelectronic applications such as ultraviolet (UV) laser, field-effect transistor, solar cells, gas sensor, UV photodetector, light-emitting diode, and nano power generators. Recently, an interesting phosphorene nanotube (PNT) designed by wrapping 2D phosphorene was reported. Topological material Bi2Se3/Bi2Te3 based 1D nanotube are remained unexplored. The nanotube based field effect transistor are in further investigation in terms of gate modulation, current voltage characteristic, the negative resistance and short channel effect. Its applications in strain sensor are also extraordinarily appealing due to the intrinsic piezoelectricity of topological insulators.

Novel materials/structures aiming at applications in power generator are in further investigation. PdS_2/$NbSe_2$/NiS_2/$NiSe_2$/NbS_2/TaS_2/$TaSe_2$/$TaTe_2$ are introduced in combination to apply for the power generator. The different device structures (Heterojunctions/three-terminal structure) are proposed to account for the strain sensors. The output performance vs. various structure length/width/thickness is in further investigation.

References

[1] B. Radisavljevic, A. Radenovic, J. Brivio, V. Giacometti, and A. Kis, "Single-layer MoS2 transistors," *Nat. Nanotechnol.*, vol. 6, no. 3, pp. 147–150, Mar. 2011.

[2] M. Tosun, S. Chuang, H. Fang, A. B. Sachid, M. Hettick, Y. Lin, Y. Zeng, and A. Javey, "High-Gain Inverters Based on WSe2 Complementary Field-Effect Transistors," *ACS Nano*, vol. 8, no. 5, pp. 4948–4953, May 2014.

[3] G.-H. Lee, Y.-J. Yu, X. Cui, N. Petrone, C.-H. Lee, M. S. Choi, D.-Y. Lee, C. Lee, W. J. Yoo, K. Watanabe, T. Taniguchi, C. Nuckolls, P. Kim, and J. Hone, "Flexible and Transparent MoS2 Field-Effect Transistors on Hexagonal Boron Nitride-Graphene Heterostructures," *ACS Nano*, vol. 7, no. 9, pp. 7931–7936, Sep. 2013.

[4] W. Li, G. Zhang, M. Guo, and Y.-W. Zhang, "Strain-tunable electronic and transport properties of MoS2 nanotubes," *Nano Res.*, vol. 7, no. 4, pp. 518–527, Jan. 2015.

[5] A. Castellanos-Gomez, M. Poot, G. A. Steele, H. S. J. van der Zant, N. Agraït, and G. Rubio-Bollinger, "Elastic properties of freely suspended MoS2 nanosheets," *Adv. Mater.*, vol. 24, no. 6, pp. 772–775, Feb. 2012.

[6] K. Liu, Q. Yan, M. Chen, W. Fan, Y. Sun, J. Suh, D. Fu, S. Lee, J. Zhou, S. Tongay, J. Ji, J. B. Neaton, and J. Wu, "Elastic Properties of Chemical-Vapor-Deposited Monolayer MoS2, WS2, and Their Bilayer Heterostructures," *Nano Lett.*, vol. 14, no. 9, pp. 5097–5103, Sep. 2014.

[7] G. López-Polín, C. Gómez-Navarro, V. Parente, F. Guinea, M. I. Katsnelson, F. Pérez-Murano, and J. Gómez-Herrero, "Increasing the elastic modulus of graphene by controlled defect creation," *Nat. Phys.*, vol. 11, no. 1, pp. 26–31, Jan. 2015.

[8] J.-U. Lee, D. Yoon, and H. Cheong, "Estimation of Young's Modulus of Graphene by Raman Spectroscopy," *Nano Lett.*, vol. 12, no. 9, pp. 4444–4448, Sep. 2012.

[9] S. R. Anton and H. A. Sodano, "A review of power harvesting using piezoelectric materials (2003?2006)," *Smart Mater. Struct.*, vol. 16, no. 3, p. R1, 2007.

[10] S.-H. Shin, M. H. Lee, J.-Y. Jung, J. H. Seol, and J. Nah, "Piezoelectric performance enhancement of ZnO flexible nanogenerator by a CuO–ZnO p–n junction formation," *J. Mater. Chem. C*, vol. 1, no. 48, pp. 8103–8107, Nov. 2013.

[11] S.-H. Shin, Y.-H. Kim, M. H. Lee, J.-Y. Jung, J. H. Seol, and J. Nah, "Lithium-Doped Zinc Oxide Nanowires–Polymer Composite for High Performance Flexible Piezoelectric Nanogenerator," *ACS Nano*, vol. 8, no. 10, pp. 10844–10850, Oct. 2014.

[12] "Solvent-assisted optimal BaTiO3 nanoparticles-polymer composite cluster formation for high performance piezoelectric nanogenerators. - PubMed - NCBI." [Online]. Available: http://www.ncbi.nlm.nih.gov/pubmed/25392282. [Accessed: 15-Jun-2016].

[13] Z. L. Wang and J. Song, "Piezoelectric Nanogenerators Based on Zinc Oxide Nanowire Arrays," *Science*, vol. 312, no. 5771, pp. 242–246, Apr. 2006.

[14] M.-P. Lu, J. Song, M.-Y. Lu, M.-T. Chen, Y. Gao, L.-J. Chen, and Z. L. Wang, "Piezoelectric Nanogenerator Using p-Type ZnO Nanowire Arrays," *Nano Lett.*, vol. 9, no. 3, pp. 1223–1227, Mar. 2009.

[15] S. Chandratre and P. Sharma, "Coaxing graphene to be piezoelectric," *Appl. Phys. Lett.*, vol. 100, no. 2, p. 23114, Jan. 2012.

[16] F. Guinea, M. I. Katsnelson, and A. K. Geim, "Energy gaps and a zero-field quantum Hall effect in graphene by strain engineering," *Nat. Phys.*, vol. 6, no. 1, pp. 30–33, Jan. 2010.

[17] A. W. Cummings, A. Cresti, and S. Roche, "Quantum Hall effect in polycrystalline graphene: The role of grain boundaries," *Phys. Rev. B*, vol. 90, no. 16, p. 161401, Oct. 2014.

[18] N. Lu, Z. Li, and J. Yang, "Electronic Structure Engineering via On-Plane Chemical Functionalization: A Comparison Study on Two-Dimensional Polysilane and Graphane," *J. Phys. Chem. C*, vol. 113, no. 38, pp. 16741–16746, Sep. 2009.

[19] A. Arab and Q. Li, "Anisotropic thermoelectric behavior in armchair and zigzag mono- and fewlayer MoS2 in thermoelectric generator applications," *Sci. Rep.*, vol. 5, p. 13706, Sep. 2015.

[20] "Ultrahigh electron mobility in suspended graphene." [Online]. Available: http://www.sciencedirect.com/science/article/pii/S0038109808001178. [Accessed: 21-Apr-2016].

[21] M. Hajlaoui, H. Sediri, D. Pierucci, H. Henck, T. Phuphachong, M. G. Silly, L.-A. de Vaulchier, F. Sirotti, Y. Guldner, R. Belkhou, and A. Ouerghi, "High Electron Mobility in Epitaxial Trilayer Graphene on Off-axis SiC(0001)," *Sci. Rep.*, vol. 6, p. 18791, Jan. 2016.

[22] F. Schwierz, "Graphene transistors," *Nat. Nanotechnol.*, vol. 5, no. 7, pp. 487–496, Jul. 2010.

[23] A. A. Balandin, S. Ghosh, W. Bao, I. Calizo, D. Teweldebrhan, F. Miao, and C. N. Lau, "Superior Thermal Conductivity of Single-Layer Graphene," *Nano Lett.*, vol. 8, no. 3, pp. 902–907, Mar. 2008.

[24] C. Lee, X. Wei, J. W. Kysar, and J. Hone, "Measurement of the Elastic Properties and Intrinsic Strength of Monolayer Graphene," *Science*, vol. 321, no. 5887, pp. 385–388, Jul. 2008.

[25] E. Kim, N. Jain, R. Jacobs-Gedrim, Y. Xu, and B. Yu, "Exploring carrier transport phenomena in a CVD-assembled graphene FET on hexagonal boron nitride," *Nanotechnology*, vol. 23, no. 12, p. 125706, 2012.

[26] S. Yu, H. D. Xiong, K. Eshun, H. Yuan, and Q. Li, "Phase transition, effective mass and carrier mobility of MoS2 monolayer under tensile strain," *Appl. Surf. Sci.*, vol. 325, pp. 27–32, Jan. 2015.

[27] K. Eshun, H. D. Xiong, S. Yu, and Q. Li, "Doping induces large variation in the electrical properties of MoS2 monolayers," *Solid-State Electron.*, vol. 106, pp. 44–49, Apr. 2015.

[28] H. Yuan, G. Cheng, L. You, H. Li, H. Zhu, W. Li, J. J. Kopanski, Y. S. Obeng, A. R. Hight Walker, D. J. Gundlach, C. A. Richter, D. E. Ioannou, and Q. Li, "Influence of Metal–MoS2 Interface on MoS2 Transistor Performance: Comparison of Ag and Ti Contacts," *ACS Appl. Mater. Interfaces*, vol. 7, no. 2, pp. 1180–1187, Jan. 2015.

[29] M. S. Fuhrer and J. Hone, "Measurement of mobility in dual-gated MoS2 transistors," *Nat. Nanotechnol.*, vol. 8, no. 3, pp. 146–147, Mar. 2013.

[30] "Mobility engineering and a metal–insulator transition in monolayer MoS2 : Nature Materials : Nature Publishing Group." [Online]. Available: http://www.nature.com/nmat/journal/v12/n9/full/nmat3687.html. [Accessed: 15-Jun-2016].

[31] E. H. Hwang and S. Das Sarma, "Acoustic phonon scattering limited carrier mobility in two-dimensional extrinsic graphene," *Phys. Rev. B*, vol. 77, no. 11, p. 115449, Mar. 2008.

[32] K. Kaasbjerg, K. S. Thygesen, and A.-P. Jauho, "Acoustic phonon limited mobility in two-dimensional semiconductors: Deformation potential and piezoelectric scattering in monolayer MoS${}_{2}$ from first principles," *Phys. Rev. B*, vol. 87, no. 23, p. 235312, Jun. 2013.

[33] S. Yu, Q. Li, and K. Eshun, "Effects of Doping, Strain and Size on the Electrical Properties of MoS2 Nanoribbons," *ECS Trans.*, vol. 64, no. 12, pp. 25–31, Aug. 2014.

[34] Q. Yue, J. Kang, Z. Shao, X. Zhang, S. Chang, G. Wang, S. Qin, and J. Li, "Mechanical and electronic properties of monolayer MoS2 under elastic strain," *Phys. Lett. A*, vol. 376, no. 12–13, pp. 1166–1170, Feb. 2012.

[35] L. Huang, Y. Li, Z. Wei, and J. Li, "Strain induced piezoelectric effect in black phosphorus and MoS2 van der Waals heterostructure," *Sci. Rep.*, vol. 5, Nov. 2015.

[36] W. Wu, L. Wang, Y. Li, F. Zhang, L. Lin, S. Niu, D. Chenet, X. Zhang, Y. Hao, T. F. Heinz, J. Hone, and Z. L. Wang, "Piezoelectricity of single-atomic-layer MoS2 for energy conversion and piezotronics," *Nature*, vol. 514, no. 7523, pp. 470–474, Oct. 2014.

[37] K.-K. Liu, W. Zhang, Y.-H. Lee, Y.-C. Lin, M.-T. Chang, C.-Y. Su, C.-S. Chang, H. Li, Y. Shi, H. Zhang, C.-S. Lai, and L.-J. Li, "Growth of Large-Area and Highly Crystalline MoS2 Thin Layers on Insulating Substrates," *Nano Lett.*, vol. 12, no. 3, pp. 1538–1544, Mar. 2012.

[38] Y.-H. Lee, X.-Q. Zhang, W. Zhang, M.-T. Chang, C.-T. Lin, K.-D. Chang, Y.-C. Yu, J. T.-W. Wang, C.-S. Chang, L.-J. Li, and T.-W. Lin, "Synthesis of Large-Area MoS2 Atomic Layers with Chemical Vapor Deposition," *Adv. Mater.*, vol. 24, no. 17, pp. 2320–2325, May 2012.

[39] A. Castellanos-Gomez, R. Roldán, E. Cappelluti, M. Buscema, F. Guinea, H. S. J. van der Zant, and G. A. Steele, "Local Strain Engineering in Atomically Thin MoS2," *Nano Lett.*, vol. 13, no. 11, pp. 5361–5366, Nov. 2013.

[40] K. He, C. Poole, K. F. Mak, and J. Shan, "Experimental Demonstration of Continuous Electronic Structure Tuning via Strain in Atomically Thin MoS2," *Nano Lett.*, vol. 13, no. 6, pp. 2931–2936, Jun. 2013.

[41] R. K. Ghosh and S. Mahapatra, "Direct Band-to-Band Tunneling in Reverse Biased Nanoribbon p-n Junctions," *IEEE Trans. Electron Devices*, vol. 60, no. 1, pp. 274–279, Jan. 2013.

[42] M. Ghorbani-Asl, N. Zibouche, M. Wahiduzzaman, A. F. Oliveira, A. Kuc, and T. Heine, "Electromechanics in MoS2 and WS2: nanotubes vs. monolayers," *Sci. Rep.*, vol. 3, Oct. 2013.

[43] W. Kohn and L. J. Sham, "Self-Consistent Equations Including Exchange and Correlation Effects," *Phys. Rev.*, vol. 140, no. 4A, pp. A1133–A1138, Nov. 1965.

[44] H. J. Monkhorst and J. D. Pack, "Special points for Brillouin-zone integrations," *Phys. Rev. B*, vol. 13, no. 12, pp. 5188–5192, Jun. 1976.

[45] J. P. Perdew, K. Burke, and M. Ernzerhof, "Generalized Gradient Approximation Made Simple," *Phys. Rev. Lett.*, vol. 77, no. 18, pp. 3865–3868, Oct. 1996.

[46] J. Kang, S. Tongay, J. Zhou, J. Li, and J. Wu, "Band offsets and heterostructures of two-dimensional semiconductors," *Appl. Phys. Lett.*, vol. 102, no. 1, p. 12111, Jan. 2013.

[47] Y. Cai, G. Zhang, and Y.-W. Zhang, "Polarity Reversed Robust Carrier Mobility in Monolayer MoS2 Nanoribbons," Oct. 2013.

[48] W. S. Yun, S. W. Han, S. C. Hong, I. G. Kim, and J. D. Lee, "Thickness and strain effects on electronic structures of transition metal dichalcogenides: 2H-MX_{2} semiconductors (M = Mo, W; X = S, Se, Te)," *Phys. Rev. B*, vol. 85, no. 3, Jan. 2012.

[49] J. Bardeen and W. Shockley, "Deformation Potentials and Mobilities in Non-Polar Crystals," *Phys. Rev.*, vol. 80, no. 1, pp. 72–80, Oct. 1950.

[50] J. Xi, M. Long, L. Tang, D. Wang, and Z. Shuai, "First-principles prediction of charge mobility in carbon and organic nanomaterials," *Nanoscale*, vol. 4, no. 15, pp. 4348–4369, Aug. 2012.

[51] S. Tongay, H. Sahin, C. Ko, A. Luce, W. Fan, K. Liu, J. Zhou, Y.-S. Huang, C.-H. Ho, J. Yan, D. F. Ogletree, S. Aloni, J. Ji, S. Li, J. Li, F. M. Peeters, and J. Wu, "Monolayer behaviour in bulk ReS2 due to electronic and vibrational decoupling," *Nat. Commun.*, vol. 5, p. 3252, Feb. 2014.

[52] D. A. Chenet, O. B. Aslan, P. Y. Huang, C. Fan, A. M. van der Zande, T. F. Heinz, and J. C. Hone, "In-Plane Anisotropy in Mono- and Few-Layer ReS2 Probed by Raman Spectroscopy and Scanning Transmission Electron Microscopy," *Nano Lett.*, vol. 15, no. 9, pp. 5667–5672, Sep. 2015.

[53] "Robust Direct Bandgap Characteristics of One- and Two-Dimensional ReS2 : Scientific Reports." [Online]. Available: http://www.nature.com/articles/srep13783. [Accessed: 22-Jan-2016].

[54] E. Liu, Y. Fu, Y. Wang, Y. Feng, H. Liu, X. Wan, W. Zhou, B. Wang, L. Shao, C.-H. Ho, Y.-S. Huang, Z. Cao, L. Wang, A. Li, J. Zeng, F. Song, X. Wang, Y. Shi, H. Yuan, H. Y. Hwang, Y. Cui, F. Miao, and D. Xing, "Integrated digital inverters based on two-dimensional anisotropic ReS2 field-effect transistors," *Nat. Commun.*, vol. 6, p. 6991, May 2015.

[55] C. Gómez-Navarro, M. Burghard, and K. Kern, "Elastic Properties of Chemically Derived Single Graphene Sheets," *Nano Lett.*, vol. 8, no. 7, pp. 2045–2049, Jul. 2008.

[56] E. Zhang, Y. Jin, X. Yuan, W. Wang, C. Zhang, L. Tang, S. Liu, P. Zhou, W. Hu, and F. Xiu, "ReS2-Based Field-Effect Transistors and Photodetectors," *Adv. Funct. Mater.*, vol. 25, no. 26, pp. 4076–4082, Jul. 2015.

[57] C. M. Corbet, C. McClellan, A. Rai, S. S. Sonde, E. Tutuc, and S. K. Banerjee, "Field Effect Transistors with Current Saturation and Voltage Gain in Ultrathin ReS2," *ACS Nano*, vol. 9, no. 1, pp. 363–370, Jan. 2015.

[58] J. Požela, K. Požela, and V. Jucienė, "Electron mobility and electron scattering by polar optical phonons in heterostructure quantum wells," *Semiconductors*, vol. 34, no. 9, pp. 1011–1015, Sep. 2000.

[59] J. Xi, M. Long, L. Tang, D. Wang, and Z. Shuai, "First-principles prediction of charge mobility in carbon and organic nanomaterials," *Nanoscale*, vol. 4, no. 15, pp. 4348–4369, Jul. 2012.

[60] R. Fivaz and E. Mooser, “Mobility of Charge Carriers in Semiconducting Layer Structures,” *Phys. Rev.*, vol. 163, no. 3, pp. 743–755, Nov. 1967.

[61] T. Kawamura and S. Das Sarma, “Phonon-scattering-limited electron mobilities in ${\mathrm{Al}}_{\mathit{x}}$${\mathrm{Ga}}_{1\mathrm{-}\mathit{x}}$As/GaAs heterojunctions,” *Phys. Rev. B*, vol. 45, no. 7, pp. 3612–3627, Feb. 1992.

[62] B. Tian, X. Zheng, T. J. Kempa, Y. Fang, N. Yu, G. Yu, J. Huang, and C. M. Lieber, “Coaxial silicon nanowires as solar cells and nanoelectronic power sources,” *Nature*, vol. 449, no. 7164, pp. 885–889, Oct. 2007.

[63] R. Walczak, J. Dziuban, A. D. T. Elliott, and P. D. Mitcheson, “26th European Conference on Solid-State Transducers, EUROSENSOR 2012Implementation of a Single Supply Pre-biasing Circuit for Piezoelectric Energy Harvesters,” *Procedia Eng.*, vol. 47, pp. 1311–1314, Jan. 2012.

[64] “Biomechanical Energy Harvesting: Generating Electricity During Walking with Minimal User Effort | Science.” [Online]. Available: http://science.sciencemag.org/content/319/5864/807. [Accessed: 16-Jun-2016].

[65] L. Chen, X. Xu, P. Zeng, J. Ma, L. Chen, X. Xu, P. Zeng, and J. Ma, “Integration of Energy Harvester for Self-Powered Wireless Sensor Network Nodes, Integration of Energy Harvester for Self-Powered Wireless Sensor Network Nodes,” *Int. J. Distrib. Sens. Netw. Int. J. Distrib. Sens. Netw.*, vol. 2014, 2014, p. e782710, Apr. 2014.

[66] “POSFET touch sensor with CMOS integrated signal conditioning electronics.” [Online]. Available: http://www.sciencedirect.com/science/article/pii/S0924424712001598. [Accessed: 15-Jun-2016].

[67] R. H. Blick and M. Grifoni, “FOCUS ON NANO-ELECTROMECHANICAL SYSTEMS,” *New J. Phys.*, vol. 7, no. 1, 2005.

[68] S. B. Lakshmanan, X. Zou, M. Hossu, L. Ma, C. Yang, and W. Chen, “Local Field Enhanced Au/CuS Nanocomposites as Efficient Photothermal Transducer Agents for Cancer Treatment,” *J. Biomed. Nanotechnol.*, vol. 8, no. 6, pp. 883–890, Dec. 2012.

[69] S.-H. Shin, M. H. Lee, J.-Y. Jung, J. H. Seol, and J. Nah, "Piezoelectric performance enhancement of ZnO flexible nanogenerator by a CuO–ZnO p–n junction formation," *J. Mater. Chem. C*, vol. 1, no. 48, pp. 8103–8107, Nov. 2013.

[70] "Probing Symmetry Properties of Few-Layer MoS2 and h-BN by Optical Second-Harmonic Generation - Nano Letters (ACS Publications)." [Online]. Available: http://pubs.acs.org/doi/abs/10.1021/nl401561r. [Accessed: 16-Jun-2016].

[71] K.-A. N. Duerloo, M. T. Ong, and E. J. Reed, "Intrinsic Piezoelectricity in Two-Dimensional Materials," *J. Phys. Chem. Lett.*, vol. 3, no. 19, pp. 2871–2876, Oct. 2012.

[72] S. Bertolazzi, J. Brivio, and A. Kis, "Stretching and Breaking of Ultrathin MoS2," *ACS Nano*, vol. 5, no. 12, pp. 9703–9709, Dec. 2011.

[73] "Two-Dimensional Nanosheets Produced by Liquid Exfoliation of Layered Materials | Science." [Online]. Available: http://science.sciencemag.org/content/331/6017/568. [Accessed: 16-Jun-2016].

[74] "Valley-selective circular dichroism of monolayer molybdenum disulphide : Nature Communications : Nature Publishing Group." [Online]. Available: http://www.nature.com/ncomms/journal/v3/n6/full/ncomms1882.html. [Accessed: 16-Jun-2016].

[75] K. F. Mak, K. He, J. Shan, and T. F. Heinz, "Control of valley polarization in monolayer MoS2 by optical helicity," *Nat. Nanotechnol.*, vol. 7, no. 8, pp. 494–498, Aug. 2012.

[76] "Valley and band structure engineering of folded MoS2 bilayers : Nature Nanotechnology : Nature Publishing Group." [Online]. Available: http://www.nature.com/nnano/journal/v9/n10/full/nnano.2014.176.html. [Accessed: 16-Jun-2016].

[77] P. Nagler, G. Plechinger, C. Schüller, and T. Korn, "Observation of anisotropic interlayer Raman modes in few-layer ReS2," *Phys. Status Solidi RRL - Rapid Res. Lett.*, vol. 9999, no. 9999, p. n/a-n/a, Nov. 2015.

[78] Y. Li, Z. Zhou, S. Zhang, and Z. Chen, "MoS2 Nanoribbons: High Stability and Unusual Electronic and Magnetic Properties," *J. Am. Chem. Soc.*, vol. 130, no. 49, pp. 16739–16744, Dec. 2008.

[79] Q. Yue, S. Chang, J. Kang, X. Zhang, Z. Shao, S. Qin, and J. Li, "Bandgap tuning in armchair MoS 2 nanoribbon," *J. Phys. Condens. Matter*, vol. 24, no. 33, p. 335501, 2012.

[80] M. T. Ong and E. J. Reed, "Engineered Piezoelectricity in Graphene," *ACS Nano*, vol. 6, no. 2, pp. 1387–1394, Feb. 2012.

[81] J. Guan, Z. Zhu, and D. Tománek, "High Stability of Faceted Nanotubes and Fullerenes of Multiphase Layered Phosphorus: A Computational Study," *Phys. Rev. Lett.*, vol. 113, no. 22, p. 226801, Nov. 2014.

[82] H. Liu, A. T. Neal, Z. Zhu, Z. Luo, X. Xu, D. Tománek, and P. D. Ye, "Phosphorene: An Unexplored 2D Semiconductor with a High Hole Mobility," *ACS Nano*, vol. 8, no. 4, pp. 4033–4041, Apr. 2014.

[83] H. Liu, A. T. Neal, M. Si, Y. Du, and P. D. Ye, "The Effect of Dielectric Capping on Few-Layer Phosphorene Transistors: Tuning the Schottky Barrier Heights," *IEEE Electron Device Lett.*, vol. 35, no. 7, pp. 795–797, Jul. 2014.

[84] S. Das, M. Demarteau, and A. Roelofs, "Ambipolar Phosphorene Field Effect Transistor," *ACS Nano*, vol. 8, no. 11, pp. 11730–11738, Nov. 2014.

[85] M. Engel, M. Steiner, and P. Avouris, "Black Phosphorus Photodetector for Multispectral, High-Resolution Imaging," *Nano Lett.*, vol. 14, no. 11, pp. 6414–6417, Nov. 2014.

[86] N. Youngblood, C. Chen, S. J. Koester, and M. Li, "Waveguide-integrated black phosphorus photodetector with high responsivity and low dark current," *Nat. Photonics*, vol. 9, no. 4, pp. 247–252, Apr. 2015.

[87] V. Tran, R. Soklaski, Y. Liang, and L. Yang, "Layer-controlled band gap and anisotropic excitons in few-layer black phosphorus," *Phys. Rev. B*, vol. 89, no. 23, p. 235319, Jun. 2014.

[88] A. J. H. M. Ankit Jain, "Strongly anisotropic in-plane thermal transport in single-layer black phosphorene," *Sci. Rep.*, vol. 5, p. 8501, 2015.

[89] H. Guo, N. Lu, J. Dai, X. Wu, and X. C. Zeng, "Phosphorene Nanoribbons, Phosphorus Nanotubes, and van der Waals Multilayers," *J. Phys. Chem. C*, vol. 118, no. 25, pp. 14051–14059, Jun. 2014.

[90] R. Fei and L. Yang, “Strain-Engineering the Anisotropic Electrical Conductance of Few-Layer Black Phosphorus,” *Nano Lett.*, vol. 14, no. 5, pp. 2884–2889, May 2014.

[91] K. Kaasbjerg, K. S. Thygesen, and K. W. Jacobsen, “Phonon-limited mobility in n-type single-layer MoS${}_{2}$ from first principles,” *Phys. Rev. B*, vol. 85, no. 11, p. 115317, Mar. 2012.

[92] M. Brandbyge, J.-L. Mozos, P. Ordejón, J. Taylor, and K. Stokbro, “Density-functional method for nonequilibrium electron transport,” *Phys. Rev. B*, vol. 65, no. 16, p. 165401, Mar. 2002.

[93] S. Grimme, “Semiempirical hybrid density functional with perturbative second-order correlation,” *J. Chem. Phys.*, vol. 124, no. 3, p. 34108, Jan. 2006.

[94] M. J. Grote and C. Kirsch, “Dirichlet-to-Neumann boundary conditions for multiple scattering problems,” *J. Comput. Phys.*, vol. 201, no. 2, pp. 630–650, Dec. 2004.

[95] G. Makov and M. C. Payne, “Periodic boundary conditions in \textit{ab initio} calculations,” *Phys. Rev. B*, vol. 51, no. 7, pp. 4014–4022, Feb. 1995.

[96] H. N. Fernández-Escamilla, J. J. Quijano-Briones, and A. Tlahuice-Flores, “Chiral phosphorus nanotubes: structure, bonding, and electronic properties,” *Phys Chem Chem Phys*, 2016.

Biography

Sheng Yu was born in Jingzhou, Hubei, China in 1988. He received the B.S. degree in electrical engineering from Wuhan University, Wuhan, China in 2010, and the M.S. degree in Microelectronics from Wuhan University, Wuhan, China in 2013, where he is currently pursuing the Ph.D. degree in strain effect on two dimensional materials and devices.

Publications & Patents

[1] S. Yu, H. Zhu, K. Eshun, C. Shi, M. Zeng, and Q. Li, "Strain-engineering the anisotropic electrical conductance in ReS2 monolayer," *Appl. Phys. Lett.*, vol. 108, no. 19, p. 191901, May 2016.

[2] S. Yu, K. Eshun, H. Zhu, and Q. Li, "Novel Two-Dimensional Mechano-Electric Generators and Sensors Based on Transition Metal Dichalcogenides," *Sci. Rep.*, vol. 5, p. 12854, Aug. 2015.

[3] S. Yu, H. D. Xiong, K. Eshun, H. Yuan, and Q. Li, "Phase transition, effective mass and carrier mobility of MoS2 monolayer under tensile strain," *Appl. Surf. Sci.*, vol. 325, pp. 27–32, Jan. 2015.

[4] S. Yu, H. Zhu, K. Eshun, A. Arab, A. Badwan, and Q. Li, "A computational study of the electronic properties of one-dimensional armchair phosphorene nanotubes," *J. Appl. Phys.*, vol. 118, no. 16, p. 164306, Oct. 2015.

[5] S. Yu, Q. Li, and K. Eshun, "Effects of Doping, Strain and Size on the Electrical Properties of MoS2 Nanoribbons," *ECS Trans.*, vol. 64, no. 12, pp. 25–31, Aug. 2014.

[6] S. Yu, X. Meng, and Y. Liu, "Investigation of microenvironment-depended photoluminescence in Eu^{3+}-implantation of GaN," *Wuhan Univ. J. Nat. Sci.*, vol. 17, no. 4, pp. 321–325, Aug. 2012.

[7] Y. Li, S. Yu, X. Meng, Y. Liu, Y. Zhao, F. qi Liu, and Z. Wang, "The effect of magnetic ordering on light emitting intensity of Eu-doped GaN," *J. Phys. Appl. Phys.*, vol. 46, no. 21, p. 215101, May 2013.

[8] K. Eshun, H. D. Xiong, S. Yu, and Q. Li, " Doping induces large variation in the electrical properties of MoS2 monolayers," *Solid-State Electron.*, vol. 106, pp. 44–49, Apr. 2015.

[9] P. Sun, F. Xue, S. Yu, X. Meng, Y. Liu, L. Zhang, "Hydrothermal Synthesis of Ce-Doped CdSe/ZnS Nanostructure for Highly Efficient Green and Red Emitting," *Nanosci. Nanotechnol. Lett.*, vol. 6, no. 10, 2014.

[10] Y. H. Liu, X. Q. Meng, S. Yu, F. Xue, and X. Wan, "The optical and structural study of a blue emitting structure with dual InGaN/GaN multiple quantum wells," *Opt. Spectrosc.*, vol. 116, no. 1, pp. 91–95, Jan. 2014.

[11] P. Sun, Y. Li, X. Meng, S. Yu, Y. Liu, F. Liu, and Z. Wang, “The magnetic field effect on optical properties of Sm-doped GaN thin films,” *J. Mater. Sci. Mater. Electron.*, vol. 25, no. 7, pp. 2974–2978, Jul. 2014.

[12] H. Yuan, G. Cheng, H. Li, H. Zhu, S. Yu, C. A. Richter, J. S. Suehle, Q. Li,. "Gate effects and current crowding in metal MoS2 contacts". (Submitted)

[13] P. Sun, Y. Liu, X. Wan, X. Meng, R. Su, and S. Yu, “Synthesis of long Ag nanowires and its application in GaN nanowires photodetector as transparent electrodes,” *J. Mater. Sci. Mater. Electron.*, vol. 26, no. 9, pp. 6787–6792, Jun. 2015.

[14] X. Q. Meng, Y. H. Liu, S. Yu., "A novel structure of white light LED without fluorescent powder and its fabrication technology", CN patent 201110270444.3, filed in Dec. 2011